International Journal of Robotics and Control Systems
Vol. 6, No. 2, 2026, pp. 1352-1388
ISSN 2775-2658
http://pubs2.ascee.org/index.php/ijrcs

Improved Sliding Mode Control for a Standalone PMSG-Based Wind Energy Conversion System with Battery Backup

Loay Sameh [a,1], Almoataz Y. Abdelaziz [a,b,2], Alfian Maarif [c,3], Mahmoud A. Mossa [d,4,*]

[a] Department of Electrical Power and Machines Engineering, Faculty of Engineering, Ain Shams University, Cairo, Egypt
[b] Faculty of Engineering and Technology, Future University in Egypt, Cairo, 11835, Egypt
[c] Department of Electrical Engineering, Universitas Ahmad Dahlan, Yogyakarta, Indonesia
[d] Electrical Engineering Department, Faculty of Engineering, Minia University 61111, Minia, Egypt
[1] loay.sameh@outlook.com; [2] almoataz_abdelaziz@eng.asu.edu.eg; [3] alfianmaarif@ee.uad.ac.id;
[4] mahmoud_a_mossa@mu.edu.eg
* Corresponding Author

ARTICLE INFO

Article history
Received January 29, 2026
Revised March 09, 2026
Accepted April 25, 2026

Keywords
PMSG;
FOC;
BSC;
SMC;
Energy Regulation;
Energy Storage;
Induction Motor;
Crop Watering

ABSTRACT

In this study, four advanced control schemes, Field-Oriented Control (FOC), Backstepping Control (BSC), Classical Sliding Mode Control (CSMC), and an Improved Sliding Mode Control (ISMC), are designed, implemented, and evaluated within a standalone Permanent Magnet Synchronous Generator (PMSG)-based WECS supplying an irrigation water pumping load. The proposed ISMC is explicitly formulated to suppress the chattering effect inherent in conventional sliding mode control while preserving robustness against system uncertainties and external disturbances. To ensure continuous and reliable operation during wind intermittency, a battery energy storage system is integrated, and a coordinated energy management strategy is developed to regulate power flow among the PMSG, battery, and pumping system. To objectively assess the effectiveness of each control strategy, a unified simulation framework is established in MATLAB/Simulink. The evaluation focuses on both steady-state and dynamic performance indices, namely the Total Harmonic Distortion (THD) of the PMSG three-phase stator currents and the convergence characteristics of the controlled variables. The results indicate that the proposed ISMC achieves superior harmonic suppression, yielding a THD reduction of 52% compared with FOC, 72% compared with CSMC, and 36% compared with BSC. These improvements directly reflect the enhanced switching behavior and reduced control-induced oscillations achieved by the ISMC formulation. In addition, convergence time analysis demonstrates a pronounced enhancement in transient response, with the ISMC reducing settling time by approximately 99% relative to FOC, 95% relative to CSMC, and 51% relative to BSC. This accelerated convergence confirms the effectiveness of the proposed control law in rapidly enforcing system trajectories onto the desired sliding surface. Collectively, the quantitative improvements in harmonic quality and dynamic response translate into improved power regulation and operational stability of the standalone WECS. Consequently, the proposed ISMC not only enhances current waveform quality and transient performance but also contributes to a more reliable and efficient integration of renewable energy and storage components in PMSG-based wind-driven pumping applications.

https://dx.doi.org/10.31763/ijrcs.v6i2.2591

1. Introduction

Developing and utilizing renewable energy sources for different purposes became the focus of interest during the last few decades for many fields of study due to several reasons, such as the need to reduce environmental pollution and the rising fossil fuel prices [1]. Renewable energy sources include various types like solar, wind, hydropower, geothermal, and biomass energy. By 2030, the contribution of electric energy generated by WECS is capable of reaching 20% of the world's production [2].

One of the most important fields that has benefited from renewable energy sources is agriculture. Irrigation water pumping systems can consume a significant amount of electric energy, which can be produced by WECS, especially for Isolated areas not connected to the grid, as explained in [3], [4]. Those pumping systems are composed of multiple components, beginning with the wind turbine system, followed by the generator, power converters, control units, battery, induction motor, and the water pump with a tank. Among these components, the generation unit is crucial in determining the performance of the WECS based on its type and specifications.

The main types of generators that can be used for WECS are Squirrel Cage Induction Generator (SCIG), Wound Rotor Induction Generator (WRIG), Doubly Fed Induction Generator (DFIG), Dual Stator-Winding Induction Generator (DWIG), Synchronous Generator with External Field Excitation, and Permanent Magnet Synchronous Generator (PMSG), which has many advantages such as high efficiency, enhanced power density, reduced maintenance requirements, and high power factor, which makes it a preferable choice for researchers developing WECS. Other types of generators can also be used for WECS, as explained thoroughly in [5].

WECS can be categorized into two types. Fixed speed wind turbines and Variable speed wind turbines. The second type has better performance than the first type, but to maximize the benefits gained from it, a control system is utilized to achieve maximum power point tracking (MPPT). Numerous control algorithms have been formulated to elevate the quality of the electric energy obtained from the generator. The earliest control Algorithm used for WECS was the Scalar control algorithm (SC), which manipulated the Machine's voltage or current magnitude and frequency while ignoring the magnetic field orientation inside the machine. This algorithm has been studied and implemented in works [6]-[8]. Though it is simply implemented, it suffers from several issues, such as restricted dynamic performance, inadequate torque control, and susceptibility to instability.

To overcome the weaknesses of the scalar control algorithm, the field-oriented control algorithm (FOC) was developed by Felix Blaschke for AC machines, which endowed AC machine drives with features comparable to those of DC drives [9]. FOC was adopted, and control systems based on it were developed for WECS to benefit from its noticeable advantages, such as precise torque control, wide speed range operation, improved efficiency, reduced torque ripple, and enhanced power quality. works [10]-[14] implemented the FOC algorithm by utilizing PI regulators in current control loops to manage the machine side converter MSC which resulted in improved performance of the WECS. Despite the advantages of the FOC algorithm, it faced a challenge, which is achieving the optimum Tuning of the Parameters of the PI Controllers. To deal with this challenge, works [15]-[18] developed different methods to achieve this purpose. A significant drawback is its slower reaction to dynamic changes, especially during startup and when there are variations in wind speed. This encouraged researchers to utilize other control algorithms such as Direct Power Control (DPC) and Direct Torque Control (DTC).

DPC was developed by T. Ohnishi and later improved by T. Noguchi and I. Takahachi [19]-[21]. The basis of this control strategy is the control loops for both real and imaginary power. To achieve zero phase angle operation, the DPC control algorithm regulates the imaginary power reference value $Q^* = 0$. The reference value of the real power P^* is determined by using a PI. The estimated real and imaginary power values are then compared to the reference values. DPC can be implemented without modulation by using switching tables as proposed in [22], [23]. Although DPC with switching tables facilitates fast power control, it carries notable disadvantages, especially those linked to variable switching frequencies and significant power ripples. These complications can affect harmonic filter design and necessitate high sampling frequencies for optimal performance. DPC can also be utilized with PWM, as in [24]-[26], or SVM, as in [27], [28]. Using modulation with DPC has noticeable advantages such as decreased harmonic distortion, Simple design, and rapid dynamic response.

DTC was developed by I. Takahashi and T. Noguchi [29], [30]. This control algorithm serves as a method for variable-frequency drives to control the torque, which in turn affects the speed of three-phase AC machines. This process involves estimating the machine's flux and torque through the measured voltages and currents of the machine. Similar to DPC, DTC can be used with no modulation by implementing switching tables as presented in [31]-[34], which offers various benefits, such as control structure simplicity, rapid dynamic response, but also has disadvantages, including high torque and flux ripples, along with a variable switching frequency. The complexity of the switching table may contribute to suboptimal performance in low-speed areas. DTC can be implemented with SVM as well, which is presented in [35]-[37]. DTC and SVM leverage the swift dynamic response of DTC alongside the benefits of SVM, which include lower torque ripple and a stable switching frequency.

Latterly, attention is drawn to Predictive Control algorithms (PC), which were initially developed for industrial control systems to overcome the drawbacks of PID regulators. Those algorithms predict the outcome of the system, and based on that, specific actions are taken to achieve enhanced performance of the system by using a cost function. The PC can be organized into two distinct types: The first type uses modulation such as deadbeat and Continuous Control-Set. The second type doesn’t need modulation, similar to hysteresis-based model predictive control (MPC), Trajectory tracking MPC, Direct Model Predictive Control, and Finite Control-Set MPC. WECS benefited from the various types of PC that are utilized to control the power converters. This is explained in works [38]-[40].

Two other control algorithms that achieved promising results when utilized for WECS are Sliding Mode Control (SMC) and Backstepping Control (BSC). SMC was first introduced by S. Emelyanov and V. Utkin. This technique is distinguished by its strength against uncertainties and disturbances, making it ideal for complex nonlinear systems. The primary idea revolves around creating a control law that drives the system's trajectory to 'slide' along a particular surface, known as the sliding surface, in the state space. BSC was developed by P. V. Kokotovic [41] and further developed by I. Kanellakopoulos [42] to improve the design and stabilization of controllers for a unique category of nonlinear dynamical systems. These systems are made up of subsystems that radiate from an irreducible subsystem, which can be stabilized through various methods. This recursive framework allows the designer to begin the design process with the known stable system and iteratively derive new controllers that stabilize each outer subsystem. The process concludes when the final external control is achieved. Consequently, this method is referred to as backstepping. Both SMC and BSC were implemented for WECs as detailed in [43]-[45].

SMC provides numerous benefits when utilized with a wind turbine-driven PMSG. These benefits encompass resilience to parameter uncertainties and disturbances, rapid dynamic response, and accurate tracking of intended operating points. However, it is hindered by a significant limitation referred to as “chattering.” This phenomenon denotes high-frequency oscillations of the system's state variables in proximity to the sliding surface. Different studies aimed to address the weaknesses of the SMC, such as Super twisting SMC as presented in [46] or second-order SMC as presented in [47]. Although those modifications managed to achieve a performance improvement, the presence of the signum function as part of the control law had drawbacks related to its discontinuous nature. [48] proposed a Sliding Mode controller which implemented a saturation function instead of the signum function. Even though replacing the signum function with the saturation function helped to avoid issues related to the discontinuous nature of the signum function, the saturation function also has drawbacks related to its fixed-slope boundary layer. Therefore, this paper aims to propose a control algorithm based on the fal function, which is nonlinear and continuous, to address the issues related to the signum and the saturation functions. Furthermore, the use of different controllers mentioned above in conjunction with power management for a diverse array of applications, including irrigation from a standalone energy system, is still not widely covered.

This paper studies a proposed improved sliding mode control algorithm, which aims to address the chattering issue suffered by classical sliding mode control while preserving robustness against parameter uncertainties. The proposed algorithm is implemented for the machine side converter (MSC) that governs the dynamics of PMSG, which is a part of an irrigation system powered by a wind turbine-driven PMSG. The performance of the system is evaluated while using four different control topologies for the MSC: FOC, BSC, classical SMC, and the proposed improved sliding mode control algorithm. Additionally, an effective power management strategy is designed and adopted to maintain a balanced power flow between the generated, stored, and consumed powers. MATLAB is used to test the different control algorithms. The main contributions of the present study can be presented as:

1. Unlike previous studies that focused primarily on enhancing control performance of WECS without considering end-use applications, this work uniquely integrates advanced converter control with power management for a standalone PMSG-based irrigation system.
2. The study presented a detailed comparative analysis of four control techniques-FOC, BSC, classical SMC, and improved SMC-for the machine-side converter of a PMSG-based WECS.
3. The study implemented a battery energy storage system to ensure stable and continuous operation of the irrigation system under varying wind conditions.
4. The study developed an effective power management algorithm to balance and coordinate energy flow among the PMSG, battery, and water pump.
5. Comprehensive MATLAB-based simulations are conducted to evaluate the performance of the four control strategies under identical conditions.
6. The study assessed definite key performance indicators, including total harmonic distortion (THD), settling time, and performance against parameter uncertainties to compare control effectiveness and robustness.
7. The presented study can be extended to be applied to other configurations of WECS after careful consideration of the physical and mathematical models of the utilized units.

The paper is partitioned into sections according to the following order, Section 2 presents an overall model of the system including the different elements of the system, Section 3 covers the power management system which controls the power flow among the elements of the system, Section 4 covers utilized algorithms to control the MSC, Section 5 studies the test and the results, Section 6 presents the conclusion reached finally, and presents future works.

2. Overall Model of the System

The system consists of elements shown in Fig. 1. This includes a power generation unit responsible for supplying the other parts with electrical power. This generation unit is a wind turbine-driven permanent magnet synchronous generator (PMSG). Besides the generation unit, there is a battery to store surplus energy, which improves the system's reliability. The IM is utilized to operate the water pump for irrigation purposes. The management of energy transmission between the distinct sections of the system is overseen by a management system and electronic converters, which regulate the currents and voltages to achieve the best performance of the system according to a suitable control algorithm.

2.1. Model of the Turbine

The following set of equations summarizes the model of the turbine shown in Fig. 2 [49].

$$\mathrm{P}_{aero} = \frac{1}{2}\rho_a \pi r^2 v_w^3 \tag{1}$$

The turbine operates for wind speeds that range between $v_{Cut\,in}$ and $v_{Cut\,off}$. The relation between wind speed and generated active power is illustrated in Fig. 3 as.

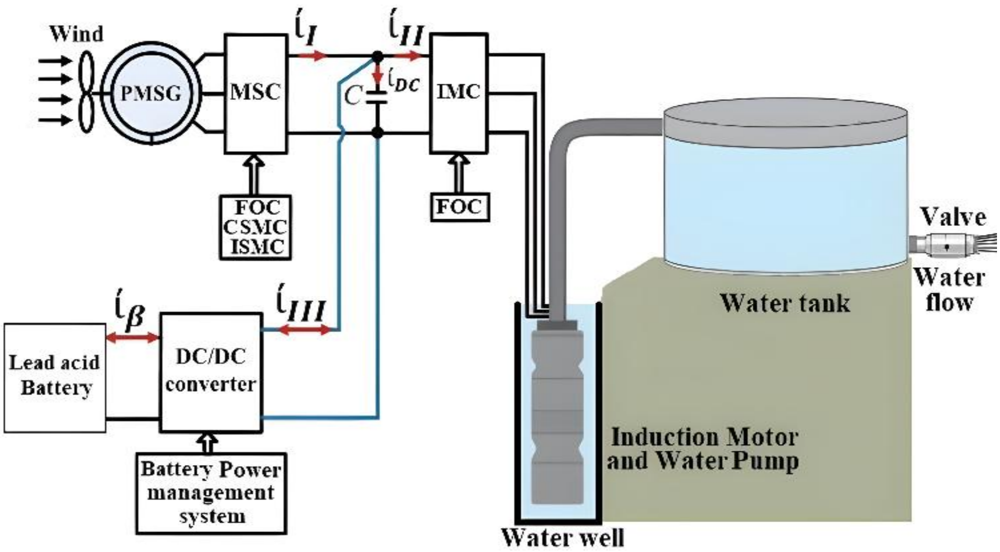

Fig. 1. Overall system schematic

$$P_T = P_{aero}\, C_p(\lambda.\beta) \tag{2}$$

$$T_T = \frac{P_T}{\Omega_T} \tag{3}$$

$$Cp = 0.53\left[\frac{151}{\lambda_i} - 0.58\beta - 0.58\beta^2 - 10\right] e^{\frac{-18{,}4}{\lambda_i}} \tag{4}$$

$$\frac{1}{\lambda_i} = \frac{1}{\lambda - 0.02\beta} - \frac{0.003}{\beta^3 + 1} \tag{5}$$

MPPT is achieved using λ_{opt} as

$$\lambda = \frac{r\Omega_T}{v_W} \tag{6}$$

$$\lambda_{opt} = \frac{r{\Omega_T}^*}{v_W} \tag{7}$$

The turbine is connected to the PMSG via a gearbox with a gear ratio G. Torque and speed of the PMSG are defined according to the following equations:

$$T_G = \frac{T_T}{G} \tag{8}$$

$$\Omega_G = G\Omega_T \tag{9}$$

$${\Omega_G}^* = G{\Omega_T}^* \tag{10}$$

$$T_T - G\,T_G - F\,G\,\Omega_T = \left(\frac{J_T}{G} + G\,J_G\right)\frac{d\Omega_T}{dt} \tag{11}$$

2.2. PMSG's Model

The following formulas are used to represent the PMSG electrical and mechanical dynamics [50]:

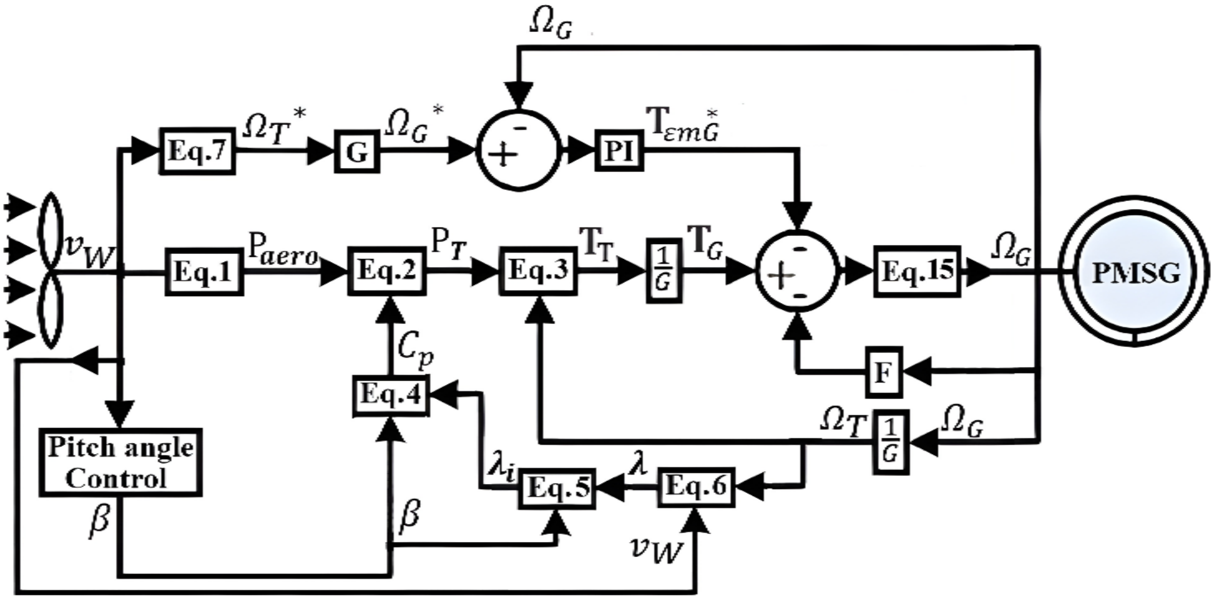

Fig. 2. Model of the turbine

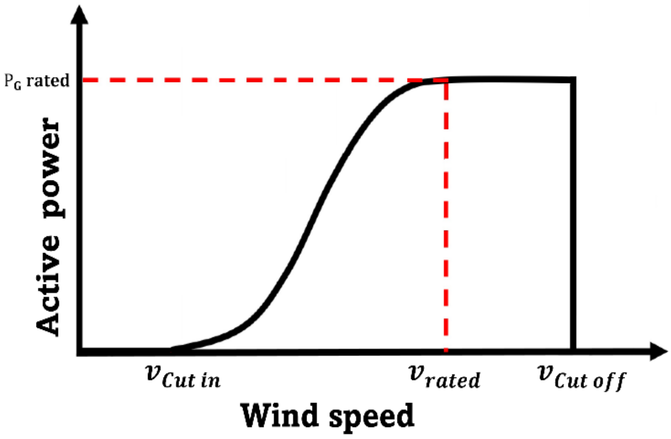

Fig. 3. Power curve of the turbine

$$\begin{cases} \nu_\delta = R_S \text{ί}_\delta + L_S \dfrac{d\text{ί}_\delta}{\mathrm{dt}} - \Omega_\varepsilon L_S \text{ί}_{\text{Ϙ}} \\ \nu_{\text{Ϙ}} = R_S \text{ί}_{\text{Ϙ}} + L_S \dfrac{d\text{ί}_{\text{Ϙ}}}{dt} + \Omega_\varepsilon L_S \text{ί}_\delta + \Omega_\varepsilon \varphi_{\mathrm{M}} \end{cases} \tag{12}$$

$$\Omega_\varepsilon = P_G \Omega_G \tag{13}$$

$$T_{\varepsilon mG} = \frac{3}{2} P_G \varphi_{\mathrm{M}} \text{ί}_{\text{Ϙ}} \tag{14}$$

$$\frac{d\Omega_G}{dt} = \frac{1}{J_G}\left(T_G - T_{\varepsilon mG} - F\Omega_G\right) \tag{15}$$

$$\begin{cases} \mathrm{P}_G = \dfrac{3}{2}\left(\nu_{\text{Ϙ}} \text{ί}_{\text{Ϙ}} + \nu_\delta \text{ί}_\delta\right) \\ \text{Ϙ}_G = \dfrac{3}{2}\left(\nu_\delta \text{ί}_{\text{Ϙ}} - \nu_{\text{Ϙ}} \text{ί}_\delta\right) \end{cases} \tag{16}$$

2.3. The Battery Model

It is implemented to store excess energy from the PMSG, which improves the reliability of the system. Numerous models have been introduced for batteries for different applications. In this paper, the RC model is employed [51], [52]. Fig. 4 illustrates the model's schematic. The following equations are used:

$$v_\beta = i_\beta R_\tau + i_1 R_\varepsilon + v_{cb} = i_\beta R_\tau + i_2 R_S + v_{cs} \tag{17}$$

$$P_\beta = v_\beta i_\beta \tag{18}$$

$$\begin{bmatrix} \dfrac{dv_{cb}}{dt} \\ \dfrac{dv_{cs}}{dt} \\ \dfrac{dv_\beta}{dt} \end{bmatrix} = \begin{bmatrix} A_{11} & A_{12} & A_{13} \\ A_{21} & A_{22} & A_{23} \\ A_{31} & A_{32} & A_{33} \end{bmatrix} \begin{bmatrix} v_{cb} \\ v_{cs} \\ v_\beta \end{bmatrix} + \begin{bmatrix} \dfrac{R_S}{C_b(R_\varepsilon + R_S)} \\ \dfrac{R_b}{C_s(R_\varepsilon + R_S)} \\ B \end{bmatrix} i_\beta \tag{19}$$

Where

$$A_{11} = \frac{-1}{C_b(R_\varepsilon + R_S)}, \quad A_{12} = \frac{1}{C_b(R_\varepsilon + R_S)}, \quad A_{13} = 0$$

$$A_{21} = \frac{1}{C_s(R_\varepsilon + R_S)}, \quad A_{22} = \frac{-1}{C_s(R_\varepsilon + R_S)}, \quad A_{23} = 0,$$

$$A_{31} = \frac{-R_S}{C_b(R_\varepsilon + R_S)^2} + \frac{R_\varepsilon}{C_s(R_\varepsilon + R_S)^2} - \frac{{R_S}^2}{C_b R_\varepsilon (R_\varepsilon + R_S)^2} + \frac{R_S}{C_s(R_\varepsilon + R_S)^2},$$

$$A_{32} = 0, \quad A_{33} = \frac{R_S}{C_b R_\varepsilon (R_\varepsilon + R_S)} - \frac{1}{C_s(R_\varepsilon + R_S)},$$

$$\mathrm{B} = \frac{{R_\varepsilon}^2}{C_b(R_\varepsilon + R_S)^2} - \frac{R_S R_\tau}{C_b(R_\varepsilon + R_S)} + \frac{R_S R_\varepsilon}{C_S(R_\varepsilon + R_S)^2} + \frac{R_\tau}{C_s(R_\varepsilon + R_S)}$$

The power flow of the battery can be regulated using a DC chopper, regulated by the management system, which is illustrated in Fig. 5.

2.4. Water Pump System

2.4.1. IM's Model and Control

The IM's model can be represented by the following relationships [41]:

$$\begin{cases} v_{\alpha\mathrm{I}} = R_{\mathrm{I}} i_{\alpha\mathrm{I}} + L_{\mathrm{I}} \dfrac{d\varphi_{\alpha\mathrm{I}}}{\mathrm{dt}} \\ v_{\beta\mathrm{I}} = R_{\mathrm{I}} i_{\beta\mathrm{I}} + L_{\mathrm{I}} \dfrac{d\varphi_{\beta\mathrm{I}}}{\mathrm{dt}} \end{cases} \tag{20}$$

$$\begin{cases} v_{\alpha\mathrm{II}} = 0 = R_{\mathrm{II}} i_{\alpha\mathrm{II}} + L_{\mathrm{II}} \dfrac{d\varphi_{\alpha\mathrm{II}}}{\mathrm{dt}} \\ v_{\beta\mathrm{II}} = 0 = R_{\mathrm{II}} i_{\beta\mathrm{II}} + L_{\mathrm{II}} \dfrac{d\varphi_{\beta\mathrm{II}}}{\mathrm{dt}} \end{cases} \tag{21}$$

$$\frac{d\Omega_{\mathrm{M}}}{dt}=\frac{1}{J_{\mathrm{M}}}\left(T_{\mathrm{M}}-T_{\varepsilon mG}-F\Omega_{\mathrm{M}}\right) \tag{22}$$

$$T_{\varepsilon m\mathrm{M}}=\frac{3P_{\mathrm{M}}\mathrm{M}_{\mathrm{M}}}{2L_{\mathrm{II}}}\left(\acute{\iota}_{\beta\mathrm{I}}\varphi_{\alpha\mathrm{II}}-\acute{\iota}_{\alpha\mathrm{I}}\varphi_{\beta\mathrm{II}}\right) \tag{23}$$

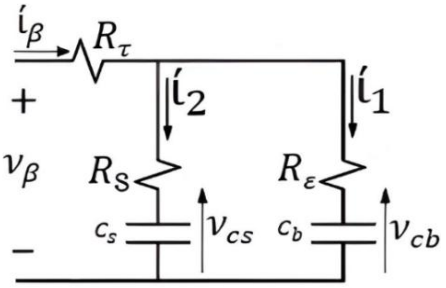

Fig. 4. The model of the battery

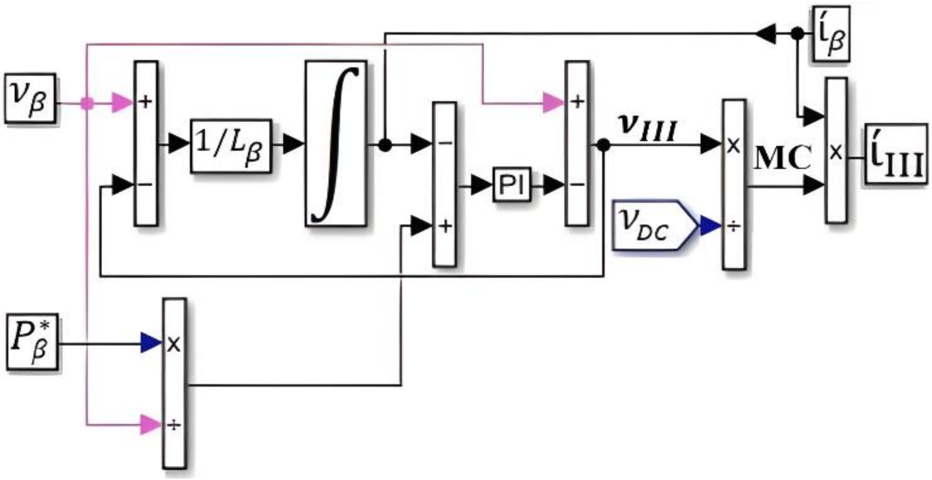

Fig. 5. Battery power management system

Electromagnetic torque and angular speed of the motor are controlled using an indirect RFOC algorithm [53] as presented in Fig. 6. This algorithm decouples the components of the flux and the torque. Rotor flux is controlled through the direct component of the stator's current, while the developed torque is controlled through quad component of the stator's current. This algorithm is based on the following equations:

$$\varphi_{\delta II}=\frac{\mathrm{M}_{\mathrm{M}}}{\tau_r S}\acute{\iota}_{\delta I} \tag{24}$$

$$T_{\varepsilon m\mathrm{M}}=\frac{3P_{\mathrm{M}}\mathrm{M}_{\mathrm{M}}}{2L_{II}}\varphi_{\delta II}\acute{\iota}_{ϙ I} \tag{25}$$

2.4.2. Water Pump and Water Tank

The water pump is coupled with the induction motor, which provides it with the needed mechanical power, the power of the pump P_Π can be calculated according to the Third Affinity Law [42] as follows:

$$P_\Pi=K_\Pi{\Omega_{\mathrm{M}}}^3=\frac{\rho_w g H_w Q_\Pi}{\eta} \tag{26}$$

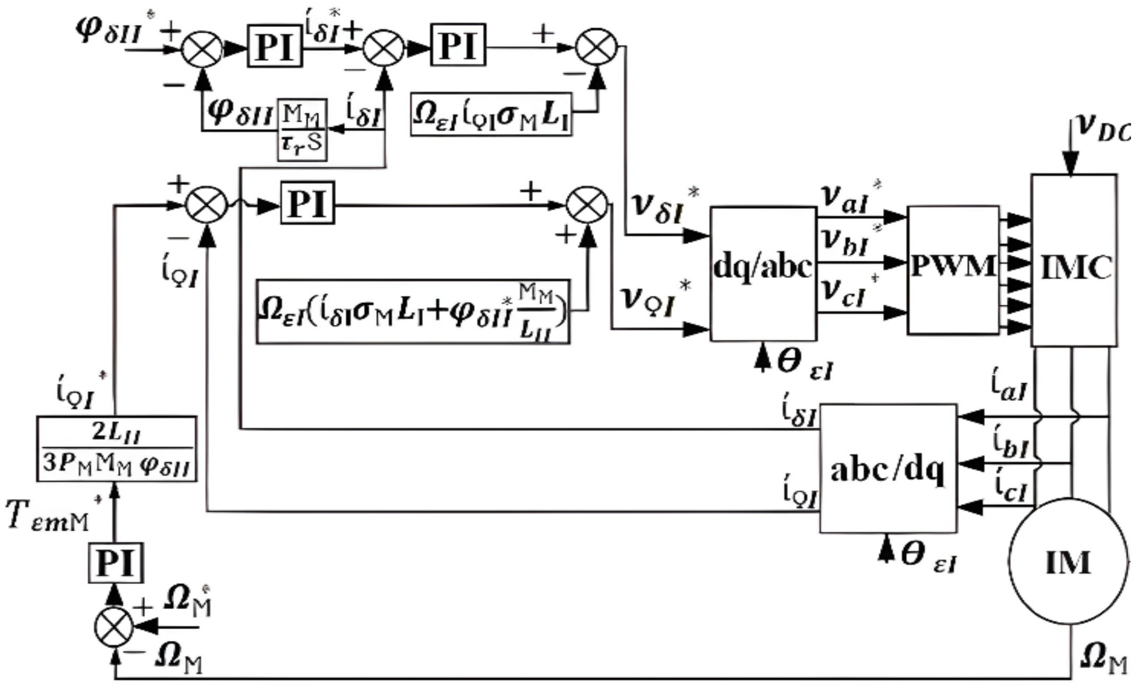

Fig. 6. General schematic of the FOC algorithm utilized for IMC

The water level inside the tank is represented using the following equation:

$$H_w = \frac{1}{A_t} \int (Q_{in} - Q_{out}) dt \tag{27}$$

Where K_Π is constant, Q_Π is the flow rate of the pump and η is its efficiency, A_t is the surface area of the tank, Q_{in} and Q_{out} are the Inflow and the outflow.

2.4.3. DC Link and Power Converters

The DC link plays a vital role in the system because it's the gate through which power is transferred among the different components of the system. The energy stored in the DC can be regulated by controlling the MSC, IMC, and the DC/DC converter to preserve the DC link voltage at the reference value.

Neglecting the losses of the converters and the DC link. The output DC current of the MSC (i_{I}) and the DC current withdrawn by IMC (i_{II}) are defined as:

$$\begin{cases} i_{\mathrm{I}} = i_\delta \dfrac{v_\delta{}^*}{v_{DC}} + i_Q \dfrac{v_Q{}^*}{v_{DC}} \\ i_{\mathrm{II}} = i_{\delta\mathrm{I}} \dfrac{v_{\delta\mathrm{I}}{}^*}{v_{DC}} + i_{Q\mathrm{I}} \dfrac{v_{Q\mathrm{I}}{}^*}{v_{DC}} \end{cases} \tag{28}$$

Therefore, the DC link voltage [54] is defined as:

$$C \frac{dv_{DC}}{\mathrm{dt}} = i_{DC} = i_{\mathrm{I}} + i_{\mathrm{III}} - i_{\mathrm{II}} \tag{29}$$

The relation between the current of the battery and the current supplied by the DC/DC converter to the DC link is presented according to:

$$\text{Modulation coefficient (MC)} = \frac{i_{III}}{i_\beta} = \frac{v_{III}}{v_{DC}} \tag{30}$$

Where $\acute{\iota}_{III}$ is the current supplied to the DC link by the DC/DC converter, and v_{III} is the voltage supplied to the DC/DC converter by the battery.

Controlling the current of the DC link is achieved using a PI regulator according to the following equation:

$$\acute{\iota}_{DC}(\mathrm{S}) = \mathrm{S}v_{DC}(\mathrm{S}) \tag{31}$$

Targeted power supplied to the DC link or withdrawn from it can be calculated according to the following:

$$P_{DC}{}^{*} = \acute{\iota}_{DC}{}^{*} v_{DC} \tag{32}$$

Currents and voltages of the DC link and the converters are shown in Fig. 7.

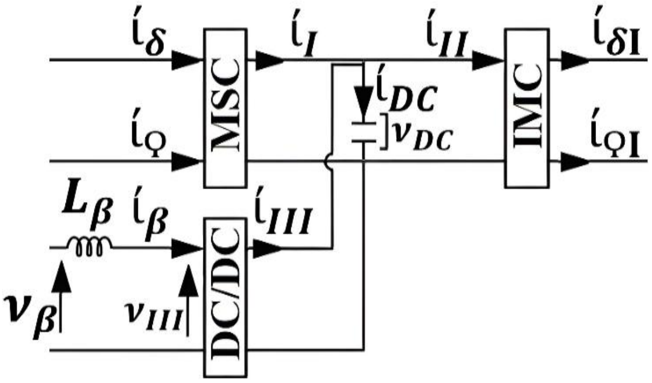

Fig. 7. The DC link and the converters

3. Power Management System

The power management system is used to control the power flow among the different components of the system to achieve balance between the power produced by the PMSG and the power consumed by the IM while utilizing the energy stored in the battery to cover the possible shortages or in case of having surplus power, the excess power can be utilized to recharge the battery, while maintaining the voltage of the DC link near the reference value. This is achieved through three steps.

The first step is taking measurements from the system, including the water level inside the tank, wind speed, power produced by the generator, the state of charge of the battery, current and voltage supplied by the battery, voltage of the DC link, and the rotational speed of the induction motor.

In order to reach the desired water level inside the tank $H_w{}^{*}$, while maintaining the SOC of the battery within the permissible range ($SOC_{Min} < SOC < SOC_{Max}$) and the voltage of the DC link at the reference value, the second step is to produce the reference signals for the control algorithms implemented for the Converters, which regulate the currents and the voltages of the PMSG using TSR method, the DC link using PI regulators, The targeted power designated to the battery and the IM is calculated according to preset operation modes depending on the current water level inside the tank, the available generated power from the PMSG, SOC of the battery and the reference power of the DC link.

The third step is to produce the switching signals which will control the MSC, the bi-directional DC/DC converter, which is used to charge the battery or extract power from it, and the inverter of the induction motor. The operation modes can be explained as follows:

3.1. Operation Mode No. 1

The water tank is full $H_w = H_w{}^{*}$, and the battery is fully charged $SOC = SOC_{Max}$. In this case, the energy generated by PMSG is neither used by the battery nor the IM.

$$\begin{cases} {P_{\Pi}}^{*} = 0 \\ {P_{\beta}}^{*} = 0 \end{cases} \tag{33}$$

3.2. Operation Mode No. 2

The water tank is full $H_w = {H_w}^{*}$, but the battery is not fully charged $SOC < SOC_{Max}$. In this case, the energy generated by PMSG is utilized to charge the battery.

$$\begin{cases} {P_{\Pi}}^{*} = 0 \\ {P_{\beta}}^{*} = P_G + {P_{DC}}^{*} \end{cases} \tag{34}$$

3.3. Operation Mode No. 3

The water tank is not full $H_w < {H_w}^{*}$, $\mathrm{P}_{\boldsymbol{G}} > \mathbf{0}$ and energy generated by the PMSG is adequate for the IM, while the energy storage element is not fully charged $SOC < SOC_{Max}$.

$$\begin{cases} {P_{\Pi}}^{*} = P_{\Pi\_nom} \\ {P_{\beta}}^{*} = P_G - P_{\Pi\_nom} + {P_{DC}}^{*} \end{cases} \tag{35}$$

3.4. Operation mode No. 4

The water tank is not full $H_w < {H_w}^{*}$, $\mathrm{P}_{\boldsymbol{G}} > \mathbf{0}$ and energy generated by the PMSG is adequate for the IM, while the energy storage element is fully charged $SOC = SOC_{Max}$.

$$\begin{cases} {P_{\Pi}}^{*} = P_{\Pi\_nom} \\ {P_{\beta}}^{*} = 0 \end{cases} \tag{36}$$

3.5. Operation Mode No. 5

The water tank is not full $H_w < {H_w}^{*}$, $\mathrm{P}_{\boldsymbol{G}} > \mathbf{0}$ while the energy generated by the PMSG is not adequate for the IM. The shortage is covered by the energy storage element.

$$\begin{cases} {P_{\Pi}}^{*} = P_{\Pi\_nom} \\ {P_{\beta}}^{*} = P_G - P_{\Pi\_nom} - {P_{DC}}^{*} \end{cases} \tag{37}$$

3.6. Operation Mode No. 6

The water tank is not full $H_w < {H_w}^{*}$, $\mathrm{P}_G = 0$, and $SOC > SOC_{Min}$. The IM is powered by the energy storage element.

$$\begin{cases} {P_{\Pi}}^{*} = P_{\Pi\_nom} \\ {P_{\beta}}^{*} = -P_{\Pi\_nom} - {P_{DC}}^{*} \end{cases} \tag{38}$$

3.7. Operation Mode No. 7

The water tank is not full $H_w < {H_w}^{*}$, $\mathrm{P}_G = 0$. while $SOC < SOC_{Min}$.

$$\begin{cases} P_{\Pi}{}^{*} = 0 \\ P_{\beta}{}^{*} = 0 \end{cases} \tag{39}$$

Fig. 8 and Fig. 9 illustrate the power management system, Operation mode selection, and power calculations.

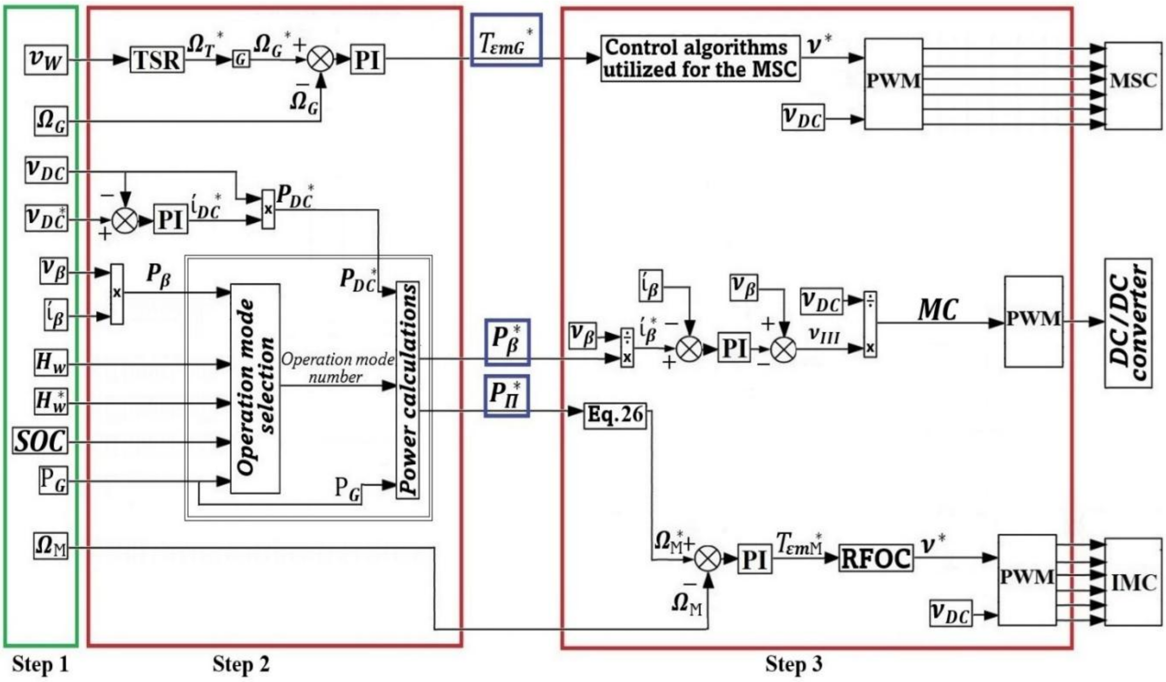

Fig. 8. Power management system

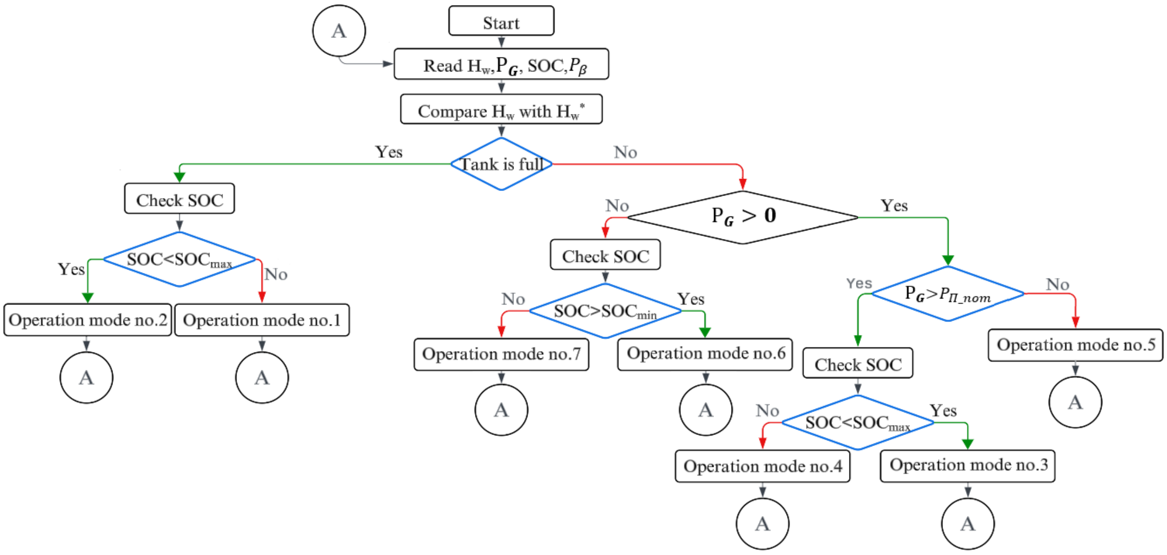

Fig. 9. Operation mode selection and power calculations

4. Control Algorithms Utilized for the MSC

To enhance the performance of the PMSG and the quality of the electric power produced by it, different algorithms (FOC, BSC, CSMC, ISMC) are implemented to control the MSC via current control loops. The concept and design of each is discussed as follows:

4.1. Field-Oriented Control

This control algorithm decouples the components of the flux and the torque of the PMSG, which makes it possible to control the PMSG in a way similar to the separately excited DC machines. The flux is controlled using the direct component of the PMSG stator current. The reference value of the Second is set to zero $\acute{\iota}_{\delta}{}^{*} = \mathbf{0}$ to achieve maximum torque per ampere (MTPA), while the quad component is used to regulate the electromagnetic torque according to the following equation:

$$T_{\varepsilon mG}{}^{*} = \frac{3}{2} P_G\, \varphi_{\mathrm{M}}\, \acute{\iota}_{\text{ϙ}}{}^{*} \tag{40}$$

Both direct and quad components of the PMSG stator current are managed using current control loops that implement PI regulators as illustrated in Fig. 10.

$$\begin{cases} \nu_{\delta}(\mathrm{S}) = \acute{\iota}_{\delta}(R_{\mathrm{S}} + \mathrm{S}L_{\mathrm{S}}) - (\Omega_{\varepsilon} L_{\mathrm{S}} \acute{\iota}_{\text{ϙ}}) \\ \nu_{\text{ϙ}}(\mathrm{S}) = \acute{\iota}_{\text{ϙ}}(R_{\mathrm{S}} + \mathrm{S}L_{\mathrm{S}}) + (\Omega_{\varepsilon} L_{\mathrm{S}} \acute{\iota}_{\delta} + \Omega_{\varepsilon}\varphi_{\mathrm{M}}) \end{cases} \tag{41}$$

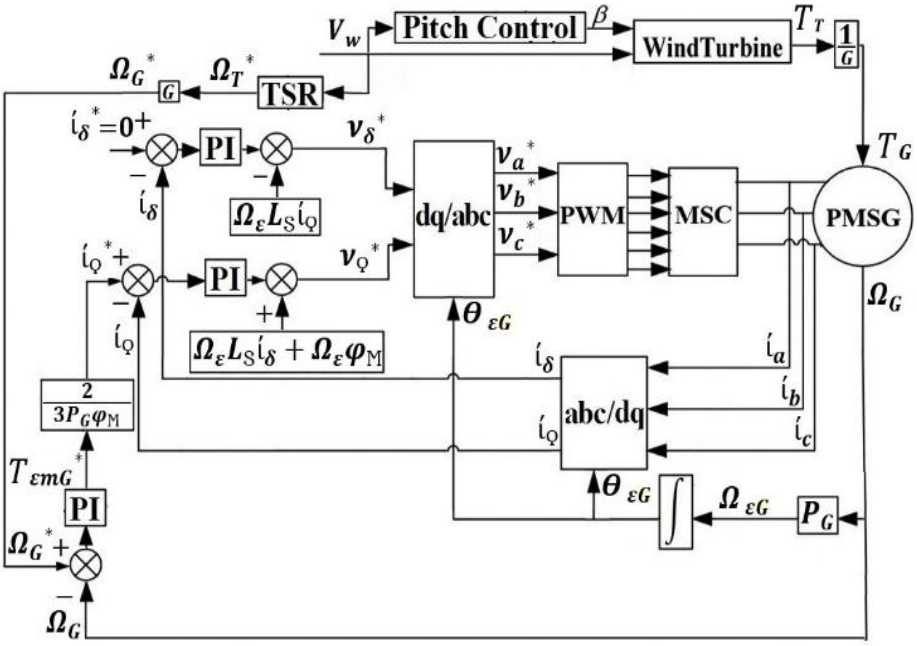

Fig. 10. General schematic of the FOC algorithm utilized for MSC

4.2. Backstepping Control

This control algorithm (Fig. 11) is designed using virtual inputs $\epsilon(\acute{\iota}_{\delta})$, $\epsilon(\acute{\iota}_{\text{ϙ}})$ and $\epsilon(\Omega_G)$ which can be expressed using the following equations:

$$\begin{cases} \epsilon(\acute{\iota}_{\delta}) = \acute{\iota}_{\delta}{}^{*} - \acute{\iota}_{\delta} \\ \epsilon(\acute{\iota}_{\text{ϙ}}) = \acute{\iota}_{\text{ϙ}}{}^{*} - \acute{\iota}_{\text{ϙ}} \\ \epsilon(\Omega_G) = \Omega_G{}^{*} - \Omega_G \end{cases} \tag{42}$$

$$\begin{cases} \dot{\epsilon}(\acute{\iota}_{\delta}) = \dfrac{d\acute{\iota}_{\delta}{}^{*}}{dt} - \dfrac{d\acute{\iota}_{\delta}}{dt} \\ \dot{\epsilon}(\acute{\iota}_{\text{ϙ}}) = \dfrac{d\acute{\iota}_{\text{ϙ}}{}^{*}}{dt} - \dfrac{d\acute{\iota}_{\text{ϙ}}}{dt} \end{cases} \tag{43}$$

$$\dot{\epsilon}(\Omega_G)=\frac{d\Omega_G{}^*}{dt}-\frac{d\Omega_G}{dt}=\frac{d\Omega_G{}^*}{dt}-\frac{1}{J_G}(T_G-\frac{3P_G}{2}\acute{\iota}_{ϙ}-F\Omega_G) \tag{44}$$

Using PMSG equations:

$$\begin{cases}\dot{\epsilon}(\acute{\iota}_\delta)=\dfrac{d\acute{\iota}_\delta{}^*}{dt}+(\dfrac{R_S}{L_S}\acute{\iota}_\delta-\Omega_\varepsilon\acute{\iota}_{ϙ}-\dfrac{\nu_\delta}{L_S})\\ \dot{\epsilon}(\acute{\iota}_{ϙ})=\dfrac{d\acute{\iota}_{ϙ}{}^*}{dt}+(\dfrac{R_S}{L_S}\acute{\iota}_{ϙ}+\Omega_\varepsilon\acute{\iota}_\delta+\dfrac{\Omega_\varepsilon\varphi_M}{L_S}-\dfrac{\nu_{ϙ}}{L_S})\end{cases} \tag{45}$$

A candidate Lyapunov function is adopted for MSC as follows:

$$\sigma=\frac{1}{2}\epsilon(\acute{\iota}_\delta)^2+\frac{1}{2}\epsilon(\acute{\iota}_{ϙ})^2+\frac{1}{2}\epsilon(\Omega_G)^2 \tag{46}$$

$$\dot{\sigma}=\dot{\epsilon}(\acute{\iota}_\delta)\epsilon(\acute{\iota}_\delta)+\dot{\epsilon}(\acute{\iota}_{ϙ})\epsilon(\acute{\iota}_{ϙ})+\dot{\epsilon}(\Omega_G)\epsilon(\Omega_G) \tag{47}$$

$$\begin{aligned}\dot{\sigma}=-\xi_\Omega\epsilon(\Omega_G)^2-\xi_\delta\epsilon(\acute{\iota}_\delta)^2-\xi_{ϙ}\epsilon(\acute{\iota}_{ϙ})^2-\frac{3P_G\epsilon(\acute{\iota}_{ϙ})\varphi_M\epsilon(\Omega_G)}{2J_G}\\+\frac{\epsilon(\acute{\iota}_\delta)[R_S\acute{\iota}_\delta-\omega_\varepsilon L_S\acute{\iota}_{ϙ}-\nu_\delta+\xi_\delta L_S\epsilon(\acute{\iota}_\delta)]}{L_S}\\+\frac{2\epsilon(\acute{\iota}_{ϙ})[\xi_\Omega J_G-F][T_G+\acute{\iota}_{ϙ}\varphi_M-F\Omega_G]}{3P_GJ_G\varphi_M}\\+\frac{\epsilon(\acute{\iota}_{ϙ})[R_S\acute{\iota}_{ϙ}+\Omega_\varepsilon L_S\acute{\iota}_\delta-\nu_{ϙ}+\xi_{ϙ}L_S\epsilon(\acute{\iota}_{ϙ})]}{L_S}\end{aligned}$$

The constants ξ_Ω, ξ_δ and $\xi_{ϙ}$ are positive, which makes $\dot{\sigma}$ negative, which satisfies the condition of Lyapunov.

Therefore, the control laws will be presented as:

$$\nu_\delta{}^*=R_S\acute{\iota}_\delta-\Omega_\varepsilon L_S\acute{\iota}_{ϙ}+\xi_\delta L_S\epsilon(\acute{\iota}_\delta) \tag{48}$$

$$\begin{aligned}\nu_{ϙ}{}^*=\frac{2L_S[\xi_\Omega J_G-F][T_G+\acute{\iota}_{ϙ}\varphi_M-F\Omega_G]}{3P_G\varphi_MJ_G}+[R_S\acute{\iota}_\delta+\Omega_\varepsilon L_S\acute{\iota}_\delta+\Omega_\varepsilon\varphi_M+\xi_{ϙ}L_S\epsilon(\acute{\iota}_{ϙ})]\\-\frac{3P_GL_S\varphi_M\epsilon(\Omega_G)}{2J_G}\end{aligned} \tag{49}$$

4.3. Proposed Sliding Mode Control

The proposed schematic shown in Fig. 12 highlights the modular structure of the control algorithm, where the switching function can be flexibly replaced (between classic and proposed) without altering the overall control architecture. Generally, the control is achieved through three major steps. First is defining a sliding surface, second is developing control laws for the direct and quad components of the stator voltage of the PMSG, and third is using a candidate Lyapunov function to examine the stability of the control system.

The sliding surface can be defined as:

$$S(\mathrm{x})=\left(\frac{d}{dt}+\delta\right)^{K-1}\epsilon(\mathrm{x}) \tag{50}$$

By choosing K=1

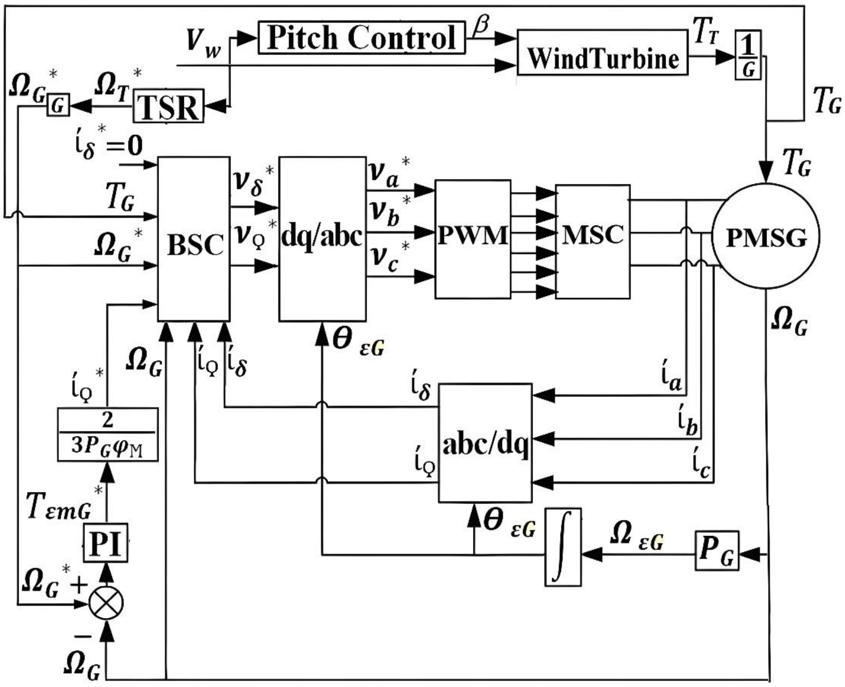

Fig. 11. General schematic of the BSC algorithm utilized for MSC

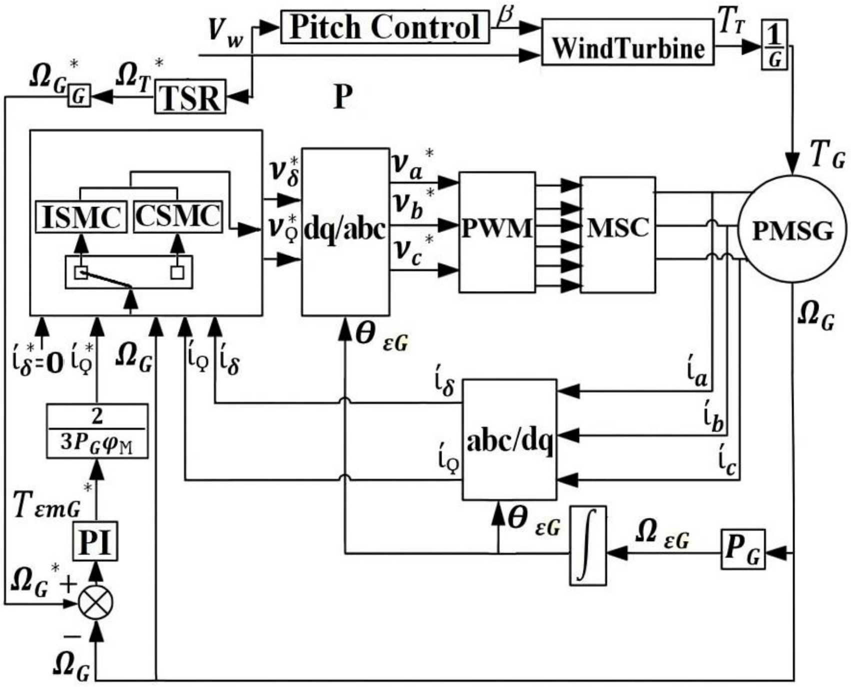

Fig. 12. General schematic of classical SMC and improved sliding mode control algorithms utilized for MSC

$$S(\mathrm{x}) = \epsilon(\mathrm{x}) = \mathrm{x}^* - \mathrm{x}^{Actual} \tag{51}$$

The control laws that will regulate the direct and quad components of the PMSG stator voltages are developed based on the following equations:

$$\begin{cases} \mathrm{S}(í_\delta) = \epsilon(í_\delta) = í_\delta{}^* - í_\delta \\ \mathrm{S}(í_Q) = \epsilon(í_Q) = í_Q{}^* - í_Q \end{cases} \tag{52}$$

By differentiating both equations:

$$\begin{cases} \dot{S}(i_\delta) = \dfrac{di_\delta{}^*}{dt} - \dfrac{di_\delta}{dt} \\ \dot{S}(i_Q) = \dfrac{di_Q{}^*}{dt} - \dfrac{di_Q}{dt} \end{cases} \tag{53}$$

Using PMSG equations:

$$\begin{cases} \dot{S}(i_\delta) = \dfrac{di_\delta{}^*}{dt} + \left(\dfrac{R_S}{L_S} i_\delta - \Omega_\varepsilon i_Q - \dfrac{\nu_\delta}{L_S}\right) \\ \dot{S}(i_Q) = \dfrac{di_Q{}^*}{dt} + (\dfrac{R_S}{L_S} i_Q + \Omega_\varepsilon i_\delta + \dfrac{\Omega_\varepsilon \varphi_M}{L_S} - \dfrac{\nu_Q}{L_S}) \end{cases} \tag{54}$$

The control law in this algorithm encompasses two parts: the first is the equivalent ν_{eq} , and the second is the switching ν_n.

So, the control law is expressed using the following equation:

$$\nu(t) = \nu_{eq}(t) + \nu_n(t) \tag{55}$$

4.3.1. The Equivalent Component ν_{eq}

This part plays a vital role in ensuring the system's operation along the specified sliding surface (manifold) once it has been achieved, effectively illustrating the ideal, continuous control necessary to uphold the reduced-order dynamics.

By substituting in (54):

$$\begin{cases} \dot{S}(i_\delta) = \dfrac{di_\delta{}^*}{dt} + (\dfrac{R_S}{L_S} i_\delta - \Omega_\varepsilon i_Q - \dfrac{\nu_{\delta eq} + \nu_{\delta n}}{L_S}) \\ \dot{S}(i_Q) = \dfrac{di_Q{}^*}{dt} + (\dfrac{R_S}{L_S} i_Q + \Omega_\varepsilon i_\delta + \dfrac{\Omega_\varepsilon \varphi_M}{L_S} - \dfrac{\nu_{Qeq} + \nu_{Qn}}{L_S}) \end{cases} \tag{56}$$

In steady-state $\dot{S}(x) = 0$, $\nu_{\delta n} = 0$ and $\nu_{Qn} = 0$.

Therefore,

$$\begin{cases} \nu_{\delta eq} = L_S \dfrac{di_\delta{}^*}{dt} + R_S i_\delta - \Omega_\varepsilon L_S i_Q \\ \nu_{Qeq} = L_S \dfrac{di_Q{}^*}{dt} + R_S i_Q + \Omega_\varepsilon L_S i_\delta + \Omega_\varepsilon \varphi_M \end{cases} \tag{57}$$

4.3.2. The Switching Component ν_n and the Control Law

The switching element of the control law plays a vital role in steering the system's state towards a defined sliding surface. It acts as a switch, shifting between two control laws according to the position of the system's state concerning the sliding surface. The switching component of the control law in classical sliding mode control is designed based on a saturation function, which is expressed using the following equation [55]:

$$Sat(X, \Delta_1) = \begin{cases} \dfrac{X}{\Delta_1} & if\ |x| \leqslant \Delta_1 \\ \mathrm{Sgn}(X) & if\ |x| > \Delta_1 \end{cases} \tag{58}$$

Therefore, the switching component of the control law can be defined as:

$$\begin{cases} v_{\delta n1} = \zeta_{\delta n1}\, Sat\big(\mathrm{S}(ί_{\delta})\big) \\ v_{Ϙ n1} = \zeta_{Ϙ n1}\, Sat\big(\mathrm{S}(ί_{Ϙ})\big) \end{cases} \tag{59}$$

And the control law can be expressed according to the following:

$$\begin{cases} v_{\delta}{}^{*} = L_{\mathrm{S}} \dfrac{dί_{\delta}{}^{*}}{dt} + R_{\mathrm{S}} ί_{\delta} - \mathit{\Omega}_{\varepsilon} L_{\mathrm{S}} ί_{Ϙ} + \zeta_{\delta n1}\, Sat\big(\mathrm{S}(ί_{\delta})\big) \\ v_{Ϙ}{}^{*} = L_{\mathrm{S}} \dfrac{dί_{Ϙ}{}^{*}}{dt} + R_{\mathrm{S}} ί_{Ϙ} + \mathit{\Omega}_{\varepsilon} L_{\mathrm{S}} ί_{\delta} + \mathit{\Omega}_{\varepsilon} \varphi_{\mathrm{M}} + \zeta_{Ϙ n1}\, Sat\big(\mathrm{S}(ί_{Ϙ})\big) \end{cases} \tag{60}$$

Unlike the saturation function, which introduces a fixed boundary layer around the sliding surface, the fal function provides a nonlinear and continuous modulation of the switching gain. This enables strong corrective action when the system state is far from the sliding surface, while significantly attenuating the control effort near the surface, leading to superior chattering suppression.

The switching component of the control law in the proposed sliding mode control is designed based on a fal function which is expressed using the following equation [56]:

$$fal(X, \alpha, \mathit{\Delta}_2) = \begin{cases} \dfrac{X}{\mathit{\Delta}_2{}^{1-\alpha}} & if\ |x| \leqslant \mathit{\Delta}_2 \\ |x|^{\alpha} Sgn(X) & if\ |x| > \mathit{\Delta}_2 \end{cases} \tag{61}$$

Therefore, the switching component of the control law can be defined as:

$$\begin{cases} v_{\delta n2} = \zeta_{\delta n2}\, fal\big(\mathrm{S}(ί_{\delta})\big) + \int \zeta_{\delta n3}\, fal\big(\mathrm{S}(ί_{\delta})\big)\, dt \\ v_{Ϙ n2} = \zeta_{Ϙ n2}\, fal\big(\mathrm{S}(ί_{Ϙ})\big) + \int \zeta_{Ϙ n3}\, fal\big(\mathrm{S}(ί_{\delta})\big)\, dt \end{cases} \tag{62}$$

And the control law can be expressed according to the following:

$$\begin{cases} v_{\delta}{}^{*} = L_{\mathrm{S}} \dfrac{dί_{\delta}{}^{*}}{dt} + R_{\mathrm{S}} ί_{\delta} - \mathit{\Omega}_{\varepsilon} L_{\mathrm{S}} ί_{Ϙ} + \zeta_{\delta n2}\, fal\big(\mathrm{S}(ί_{\delta})\big) \zeta_{\delta n2}\, fal\big(\mathrm{S}(ί_{\delta})\big) + \int \zeta_{\delta n3}\, fal\big(\mathrm{S}(ί_{\delta})\big)\, dt \\ v_{Ϙ}{}^{*} = L_{\mathrm{S}} \dfrac{dί_{Ϙ}{}^{*}}{dt} + R_{\mathrm{S}} ί_{Ϙ} + \mathit{\Omega}_{\varepsilon} L_{\mathrm{S}} ί_{\delta} + \mathit{\Omega}_{\varepsilon} \varphi_{\mathrm{M}} + \zeta_{Ϙ n2}\, fal\big(\mathrm{S}(ί_{Ϙ})\big) + \int \zeta_{Ϙ n3}\, fal\big(\mathrm{S}(ί_{\delta})\big)\, dt \end{cases} \tag{63}$$

Similar to FOC, the reference value of the direct component of the PMSG stator's current is set to zero $ί_{\delta}{}^{*} = 0$ to achieve maximum torque per ampere (MTPA), while $ί_{Ϙ}{}^{*}$ is calculated according to equation (40).

It is important to emphasize that the proposed approach does not introduce a fundamentally new reaching law structure. Instead, the novelty lies in replacing the fixed-slope boundary layer associated with the classical saturation function by a nonlinear continuous fal function. This replacement results in a state-dependent effective switching gain. For $|S| > \Delta_2$, the switching term behaves as $v_{\mathrm{n}} = \zeta |S|^{\alpha} Sgn(S)$, which implies an effective gain proportional to $|S|^{\alpha-1}$. Consequently, stronger corrective action is produced when the system state is far from the sliding surface, while the gain is automatically reduced near the surface, significantly attenuating chattering without altering the overall control structure. The stability of the controller is examined by using a candidate Lyapunov function:

$$\Upsilon = \frac{1}{2}\mathrm{S}(ί_{\delta})^{2} + \frac{1}{2}\mathrm{S}(ί_{Ϙ})^{2} \tag{64}$$

$$\dot{\Upsilon} = \dot{S}(\acute{\iota}_{\delta})S(\acute{\iota}_{\delta}) + \dot{S}(\acute{\iota}_{\text{ϙ}})S(\acute{\iota}_{\text{ϙ}}) < 0 \tag{65}$$

It is worth noting that for $0 < \alpha < 1$, when $S > \Delta_2$ The Lyapunov derivative satisfies $\dot{\Upsilon} \leq -\zeta|S|^{\alpha+1}$, which guarantees finite-time reaching of the boundary layer.

Inside the boundary region $S \leq \Delta_2$, the fal function behaves linearly, resulting in exponential convergence of the sliding variable. Therefore, the proposed controller ensures practical finite-time convergence to a small neighborhood of the sliding surface while significantly reducing chattering compared to classical saturation-based SMC.

Constants $\zeta_{\delta n1}$, $\zeta_{\text{ϙ}n1}$, $\zeta_{\delta n2}$, $\zeta_{\text{ϙ}n2}$, $\zeta_{\delta n3}$ and $\zeta_{\text{ϙ}n3}$ are positive, which makes $\dot{\Upsilon}$ negative, satisfying the condition of Lyapunov. Due to the continuous and nonlinear nature of the fal function, the time derivative of the Lyapunov function exhibits smoother convergence compared to the saturation-based SMC, providing smoother control action and reduced high-frequency oscillations while preserving Lyapunov stability.

5. Performance Evaluation Results

To evaluate the performance of each control algorithm, FOC, BSC, CSMC, and the proposed ISMC were utilized to control the MSC. A simulation was executed on MATLAB, and the results of the control algorithms were compared according to the following:

1. Parameters of the System are detailed in Table 2.
2. Wind speed is variable with min value = 1.35004 m/s and max value = 13.0994 m/s.
3. The FOC algorithm is implemented to control IMC.

5.1. The Performance of the Turbine

Fig. 13 shows the wind speed, which varies between 1.35 m/s and 13.1 m/s. The rated speed permissible by the turbine is 10.2 m/s. beyond the rated wind speed, the pitch angle control is activated to regulate the rotational speed of the turbine and the generator, which is shown in Fig. 14. Fig. 15 shows the rotational speed of the turbine. Fig. 16 shows the tip speed ratio of the wind turbine, which is maintained at an optimum value to ensure the most beneficial usage of the wind turbine under all possible fluctuations of wind speed. Fig. 17 shows the mechanical power extracted from the wind. Fig. 18 shows the power coefficient. It represents the ratio of the useful mechanical power extracted to the mechanical power of the wind. The turbine can't extract mechanical power beyond the rated value, so the power coefficient decreases when the wind speed crosses the threshold set for the pitch angle control. The zoomed parts highlight the periods [66.37-68.79] sec and [100.806-107.823] sec when wind speed exceeds the rated value.

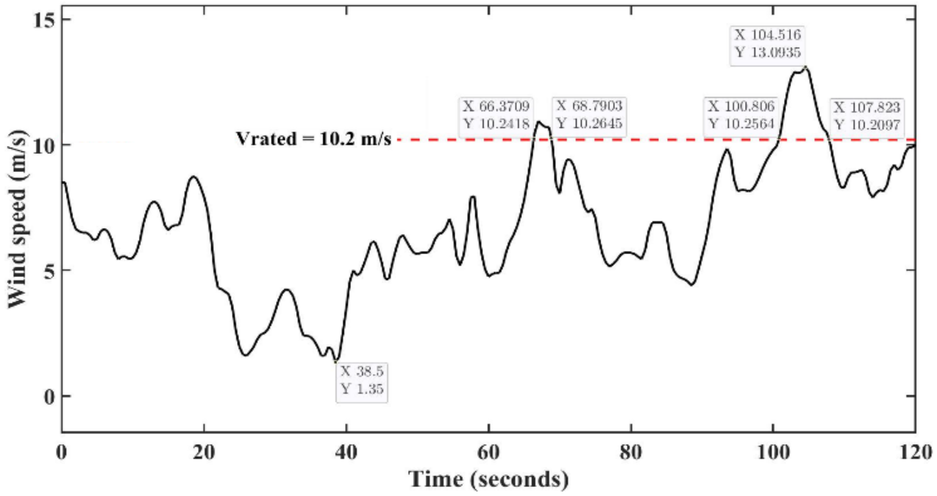

Fig. 13. Wind speed

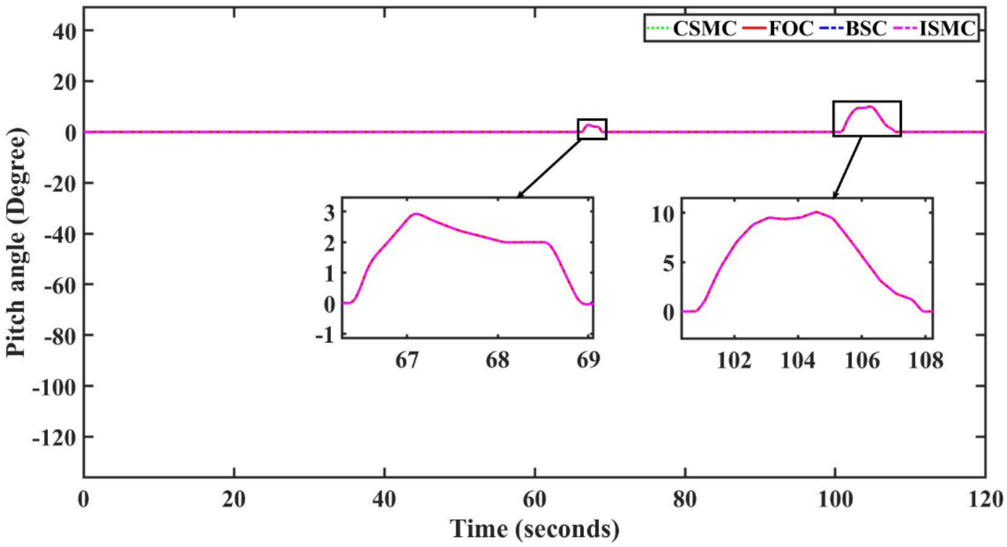

Fig. 14. Pitch angle

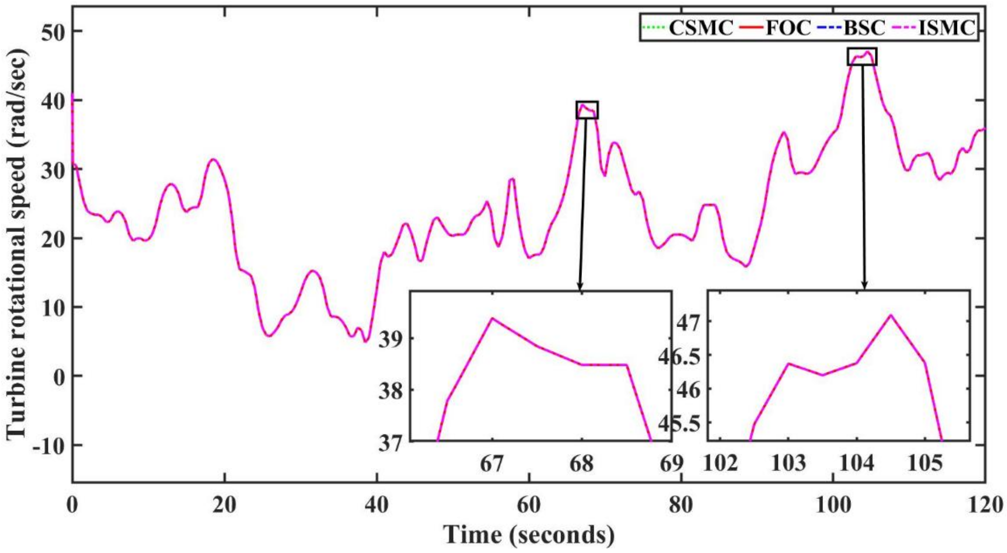

Fig. 15. Turbine rotational speed

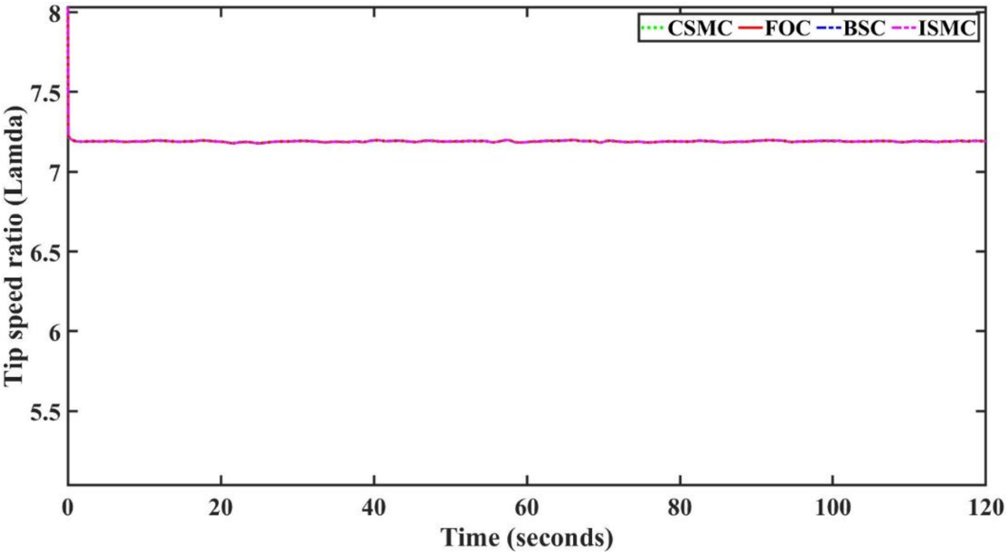

Fig. 16. Tip speed ratio

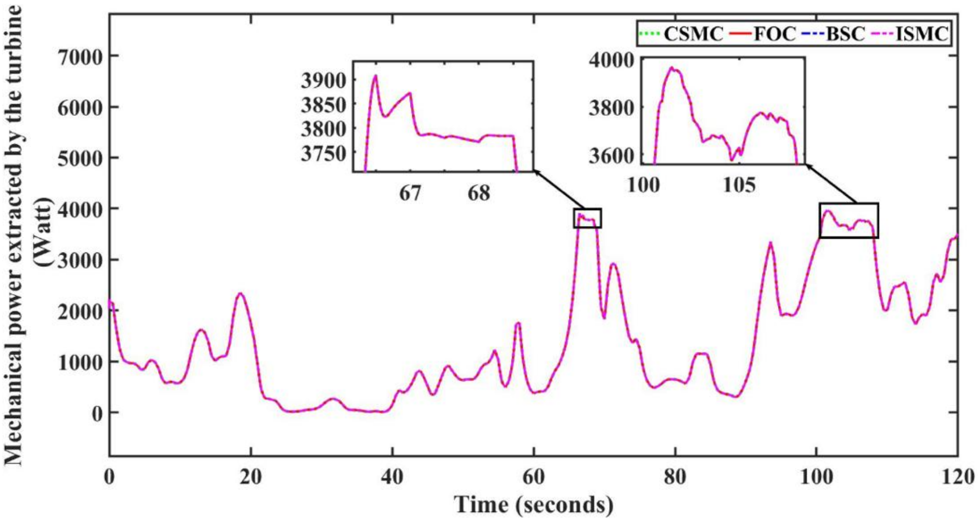

Fig. 17. Mechanical power extracted

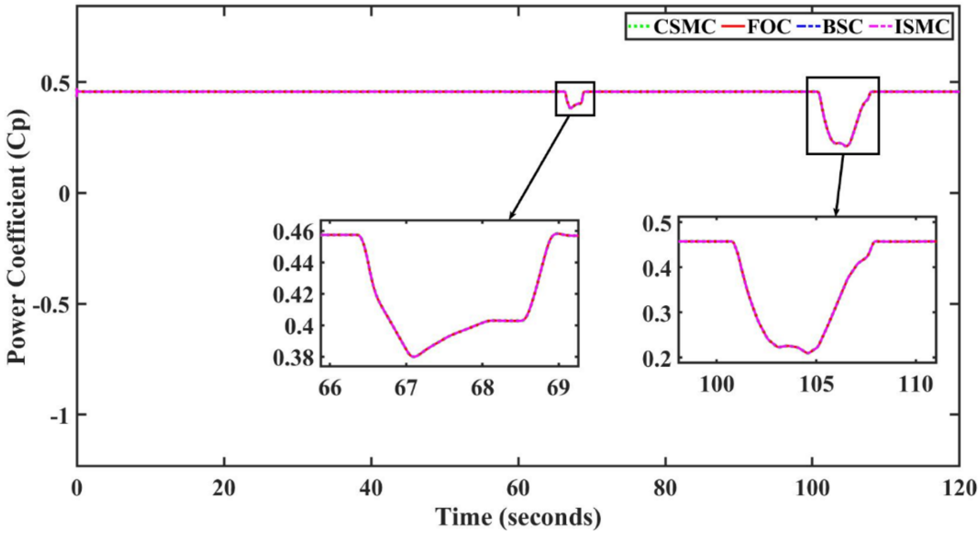

Fig. 18. Power coefficient

5.2. The Performance of the Generator

The rotational speed of the generator is shown in Fig. 19. The performance of the generator is examined by inspecting the behavior of both the direct and the quad components of the PMSG stator current, the electromagnetic torque, and the active power generated. The quad current component shown in Fig. 20 controls the electromagnetic torque and the active power generated. It reflects the variation of the wind speed. Zoomed time intervals show the behavior of the quad current component under the utilized algorithms. The first interval shows the beginning of the generation. Intervals [0-0.3], [57.5-57.85], [60-60.02], and [93.49-93.515] show moments when a sharp, sudden change of wind speed occurs. As seen, the proposed algorithm has the fastest response while maintaining minimum steady-state error.

The active power shown in Fig. 21 and the electromagnetic torque shown in Fig. 22 have a pattern similar to the quad current component. Several time intervals are zoomed to highlight the behavior of both at the beginning and when wind speed increases or decreases sharply under the four control algorithms. The proposed algorithm shows a response faster than the other algorithms, and it also has reduced oscillations and steady state error, which improves the performance of the generator.

The direct current component shown in Fig. 23 has a reference value set to zero to achieve maximum torque per ampere. As shown, it has the lowest value under the proposed control algorithm, followed by the other algorithms.

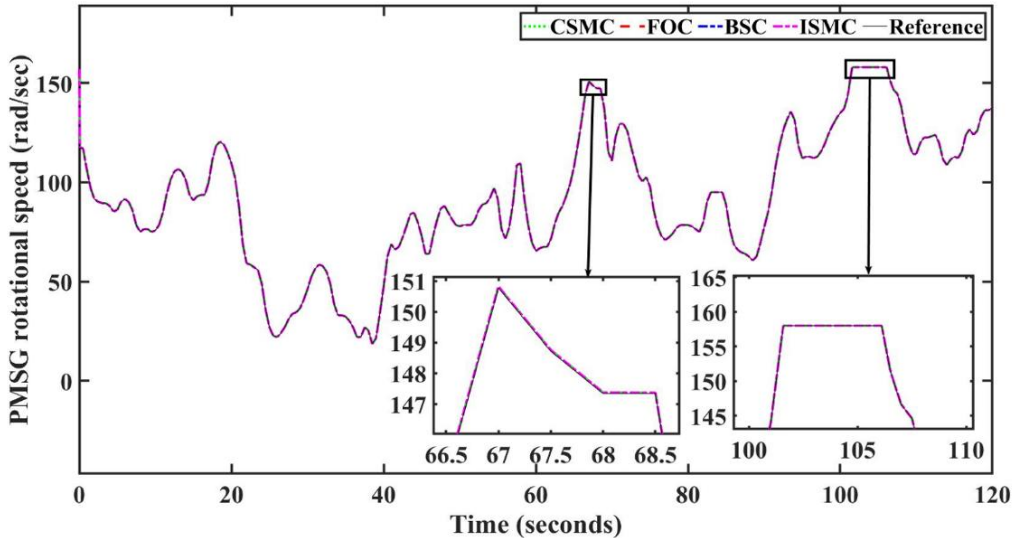

Fig. 19. Angular speed of PMSG

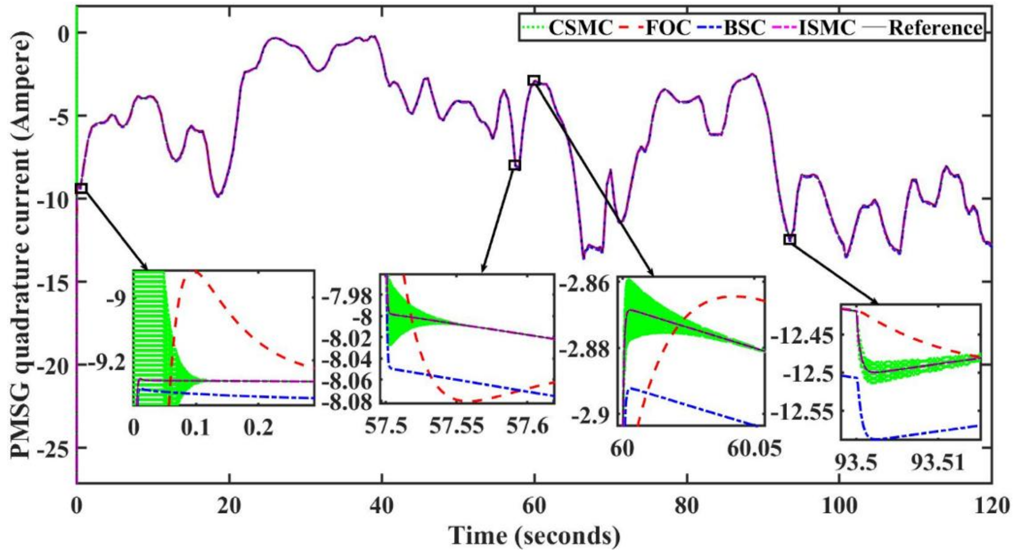

Fig. 20. Quad current component of PMSG

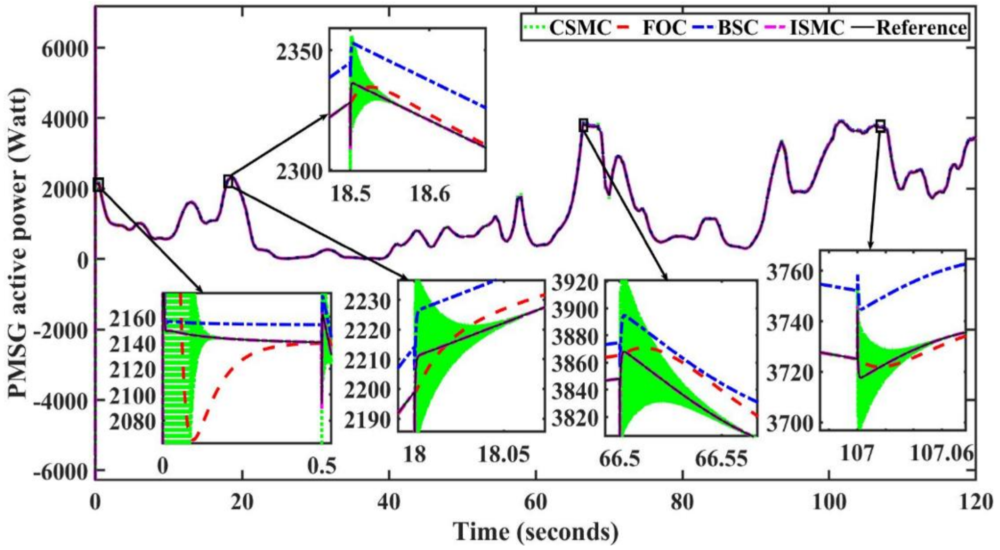

Fig. 21. PMSG active power

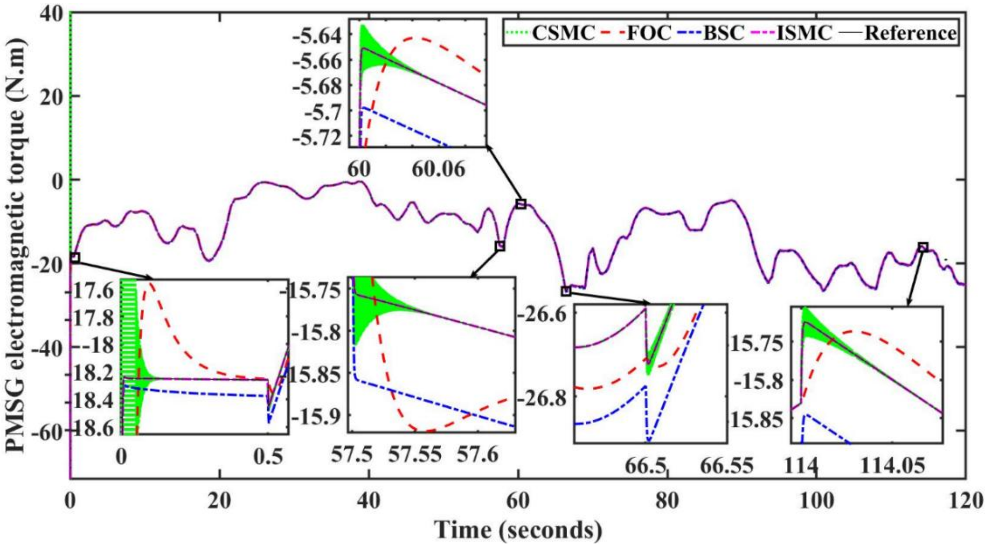

Fig. 22. PMSG electromagnetic torque

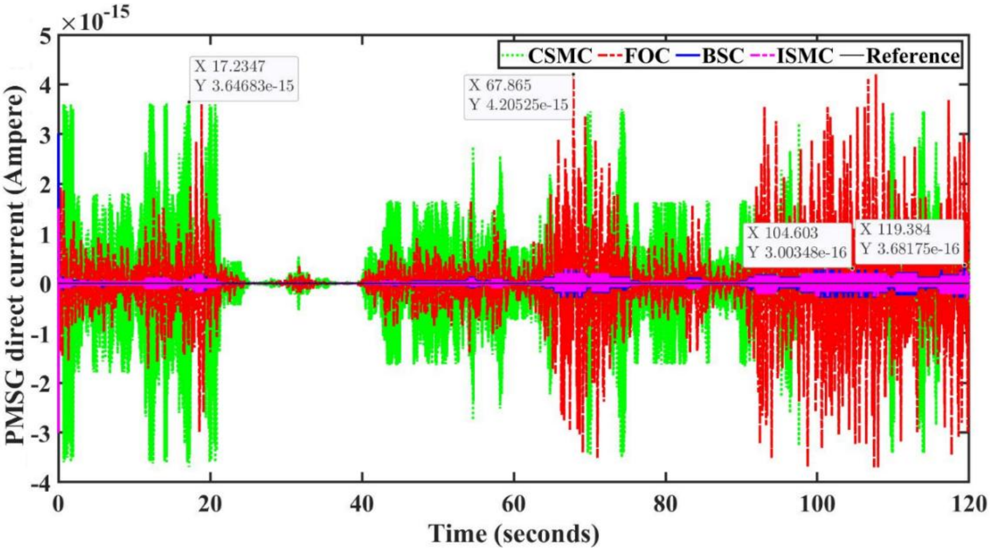

Fig. 23. Direct current component of PMSG

5.3. THD Analysis of the PMSG Stator Current

Fig. 24 shows a sample of current harmonics Analysis of PMSG three-phase stator currents under FOC, CSMC, BSC, and ISMC using FFT. The results are presented in Table 1, which shows that ISMC achieved the lowest THD.

5.4. The Effect of Parameter Uncertainties on the Performance of the Generator

To examine the robustness of the proposed algorithm against parameter variation, the quad component (Fig. 25), the active power (Fig. 26), and the electromagnetic torque (Fig. 27) were inspected during a time period while both Rs and Ls are variable. The figures show that FOC is highly sensitive to parameter variation. Its slow response becomes slower. The CSMC suffers from increased oscillations due to parameter mismatch. The BSC, on the other hand, has a faster response but with steady state error. The ISMC has the fastest response with the minimum steady state error.

5.5. The Performance of the DC Link

The voltage of the DC link shown in Fig. 28 has a reference value set to 550 V. A time interval [64.9-65.7] is zoomed and inspected. As seen, under the proposed algorithm, the DC link voltage is closer to the reference value than the other algorithms.

Table 1. Current harmonics Analysis of PMSG three-phase stator currents under FOC, CSMC, and the proposed ISMC

Phase	FOC	CSMC	BSC	ISMC
Phase (a)	Essential (4.593 A) THD (0.64 %)	Essential (4.591 A) THD (0.97 %)	Essential (4.625 A) THD (0.43 %)	Essential (4.594 A) THD (0.27 %)
Phase (b)	Essential (4.598 A) THD (0.27 %)	Essential (4.603 A) THD (0.62 %)	Essential (4.625 A) THD (0.25 %)	Essential (4.594 A) THD (0.16 %)
Phase (c)	Essential (4.589 A) THD (0.48 %)	Essential (4.600 A) THD (0.73 %)	Essential (4.623 A) THD (0.32 %)	Essential (4.593 A) THD (0.21 %)

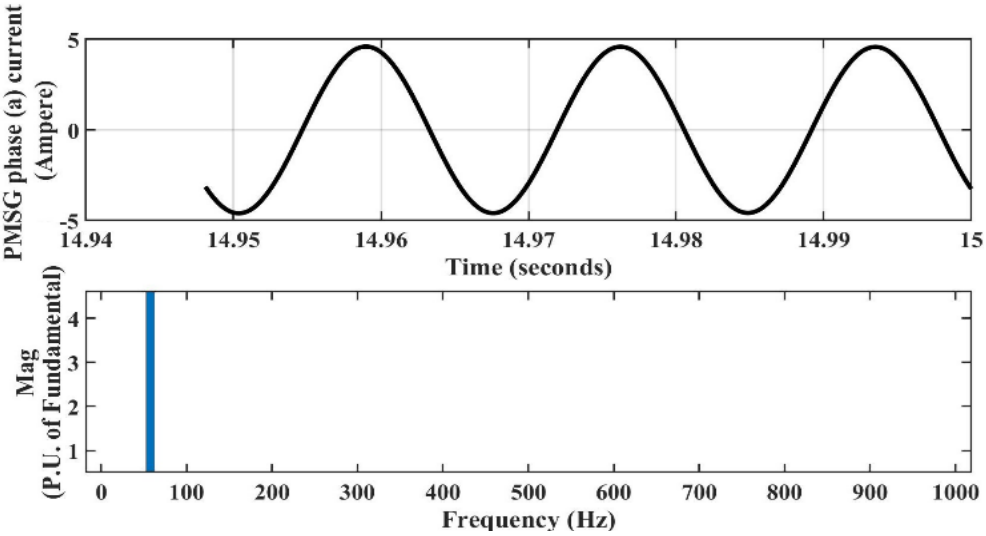

Fig. 24. Phase A under FOC

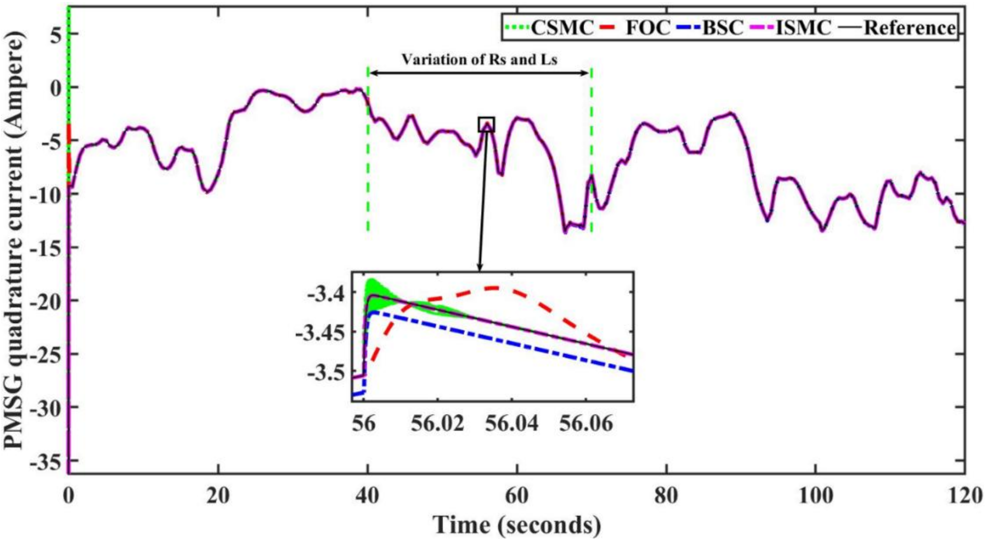

Fig. 25. Quad current component of PMSG

5.6. The performance of the Battery

To evaluate the performance of the battery under the studied algorithms, the state of charge, the voltage, the current, and the power of the battery are inspected. The state of charge is shown in Fig. 29, and the voltage is shown in Fig. 30. Several time intervals are zoomed to highlight the periods when the battery starts to get charged by surplus power from the generator, and when the battery starts to supply power to the induction motor to cover the power shortage. As seen, under the proposed algorithm, the battery starts to be charged, and starts supplying power faster than the other algorithms.

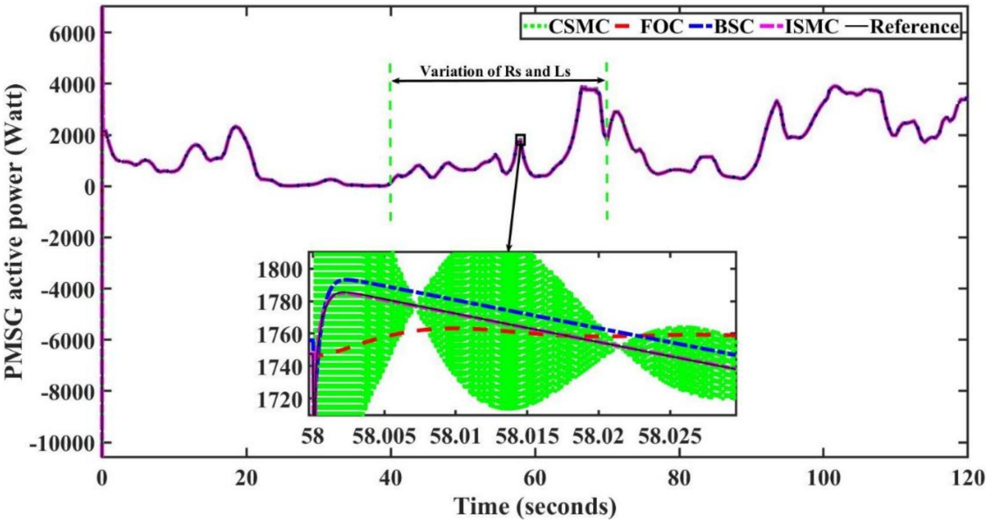

Fig. 26. PMSG active power

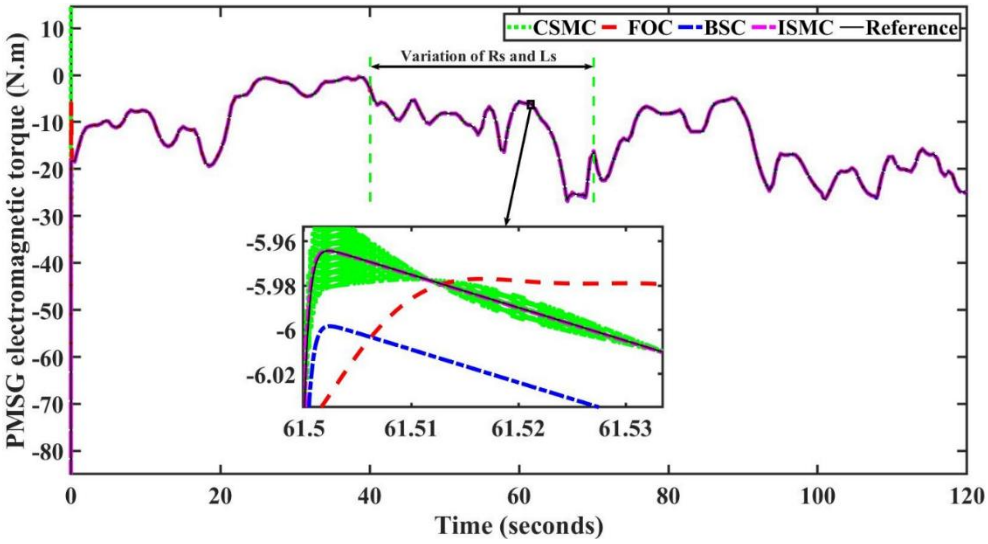

Fig. 27. PMSG electromagnetic torque

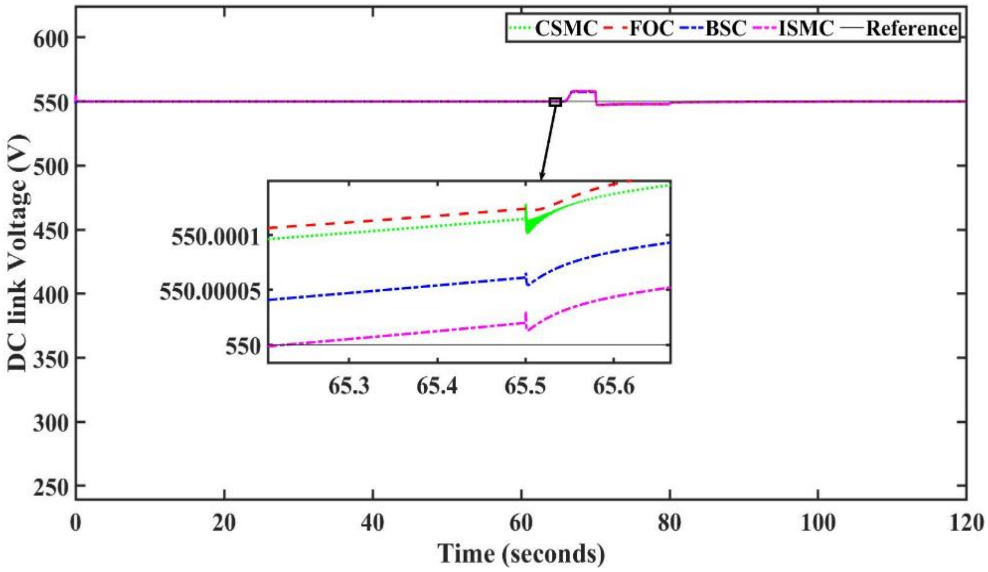

Fig. 28. DC link voltage

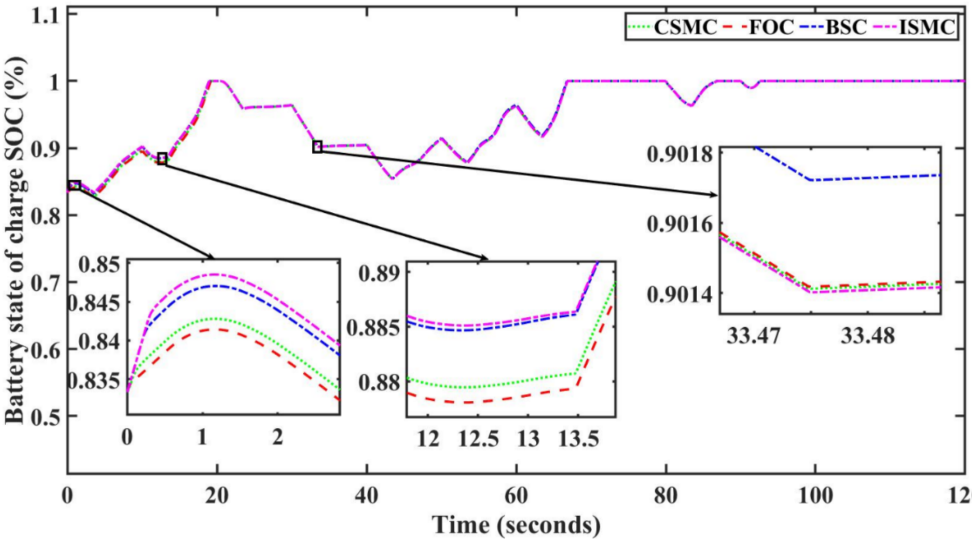

Fig. 29. Battery state of charge (%)

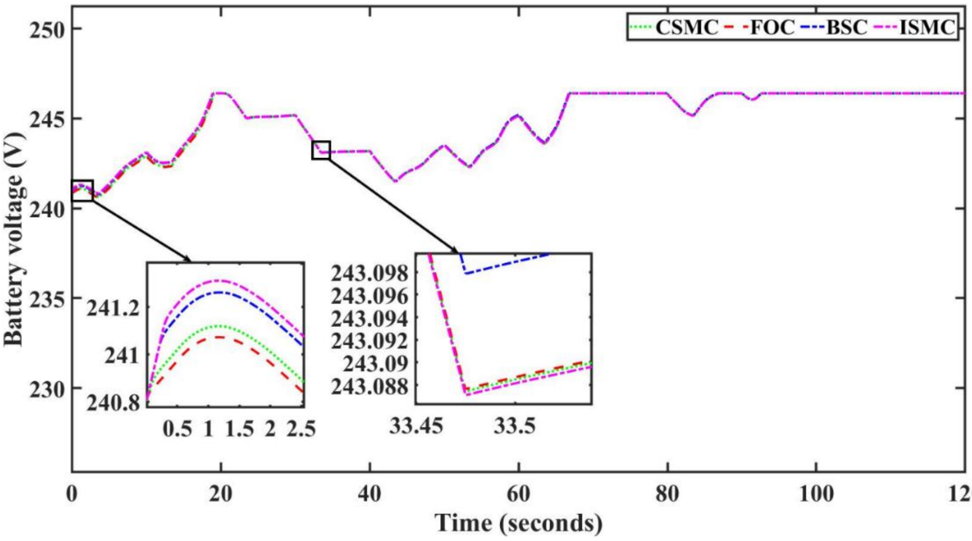

Fig. 30. Battery voltage

The current of the battery is shown in Fig. 31, and the power of the battery is shown in Fig. 32. Several time intervals are zoomed to highlight the response of the system under the studied algorithms. As seen, the proposed algorithm has a faster response than the other algorithms, and manages to solve the chattering issue suffered by the classical sliding mode control algorithm with minimum steady state error.

5.7. The Performance of the Water Pump

Fig. 33, Fig. 34, Fig. 35, Fig. 36 show the performance of the water pump. Inside the tank, the water stage is determined to be 3.5 meters. When it drops below the reference value, the water pump starts refilling it. This is done by increasing the water flow, as illustrated in Fig. 33. At the beginning, when the tank was empty, it started to fill it, but when the water level (Fig. 34) reached its reference value, the water flow was stopped to avoid overfilling the tank. When the level started to drop due to water consumption, the water pump started refilling the tank to restore the water level to the reference value. The water flow is controlled by the water pump, which is supervised by the power management system. The power it draws from the system can be observed in Fig. 36. It shows the time periods during which the water pump operates to supply the required water flow for the tank. The torque of the water pump can be seen in Fig. 35. It indicates the performance of the water pump. It can be noticed that the effectiveness of the designed power management is validated through optimizing the water stage inside the tank according to the power flow in the system.

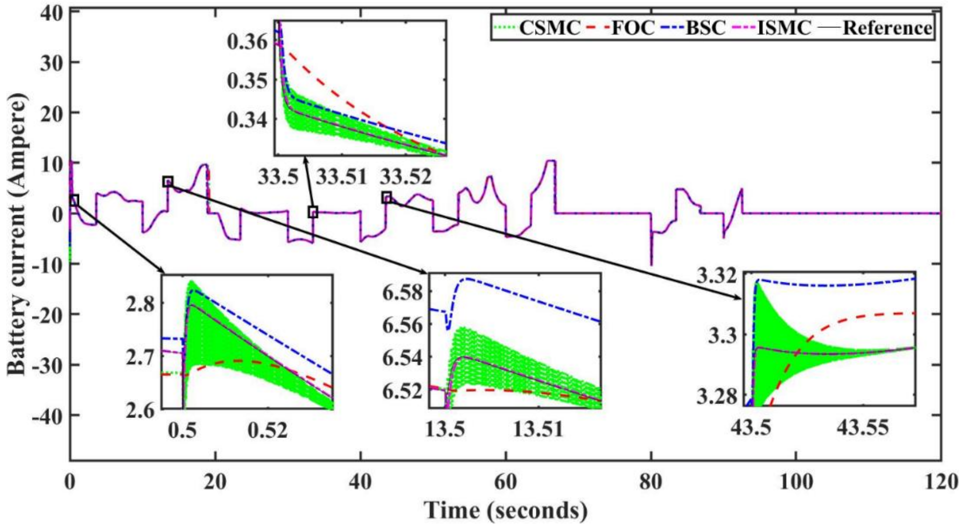

Fig. 31. Battery current

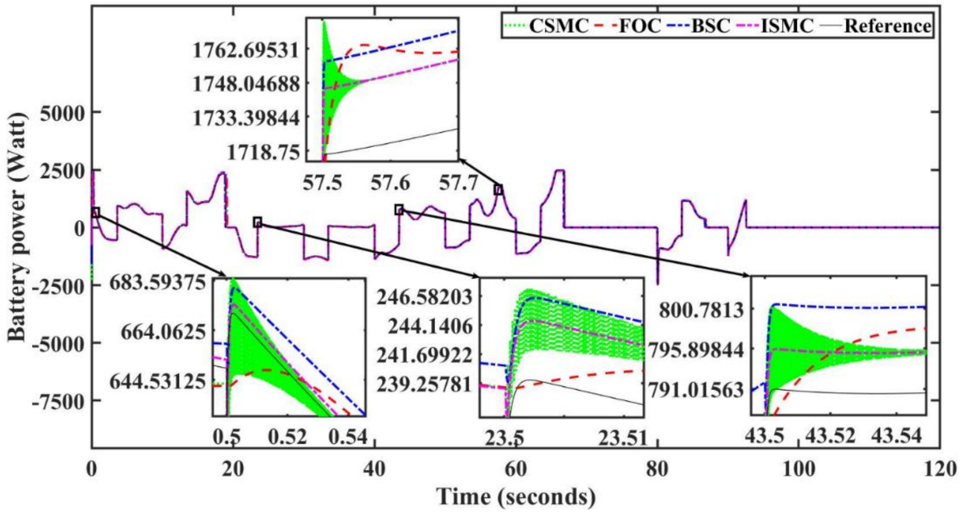

Fig. 32. Battery power

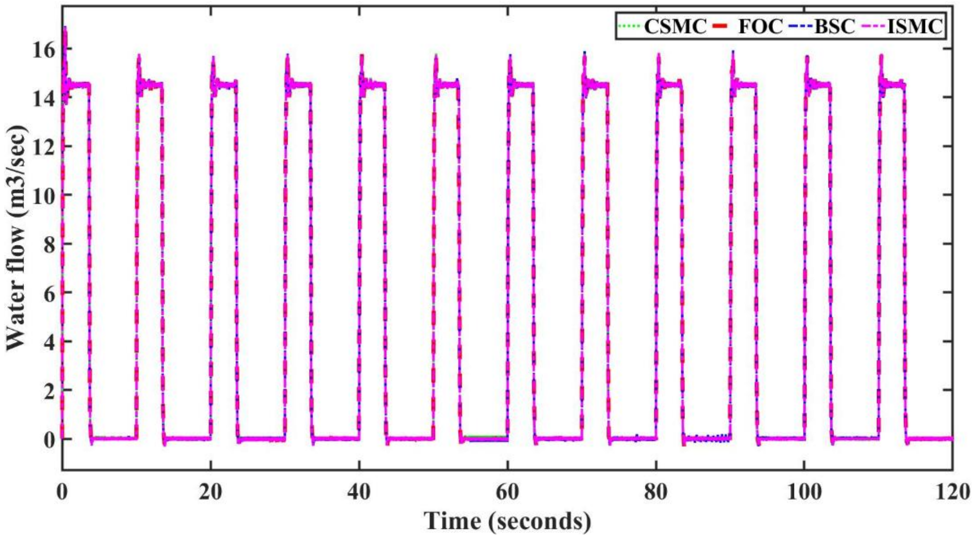

Fig. 33. Water flow

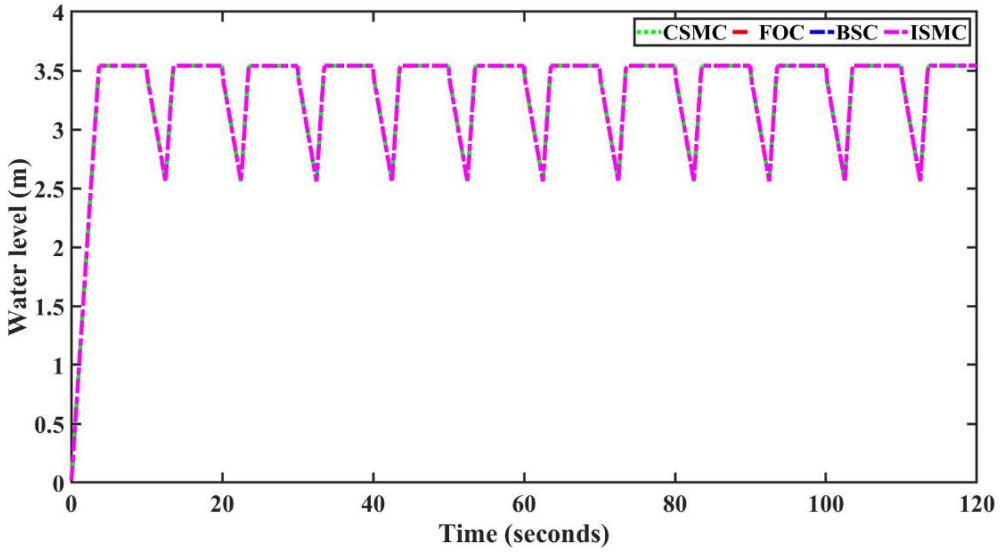

Fig. 34. Water level

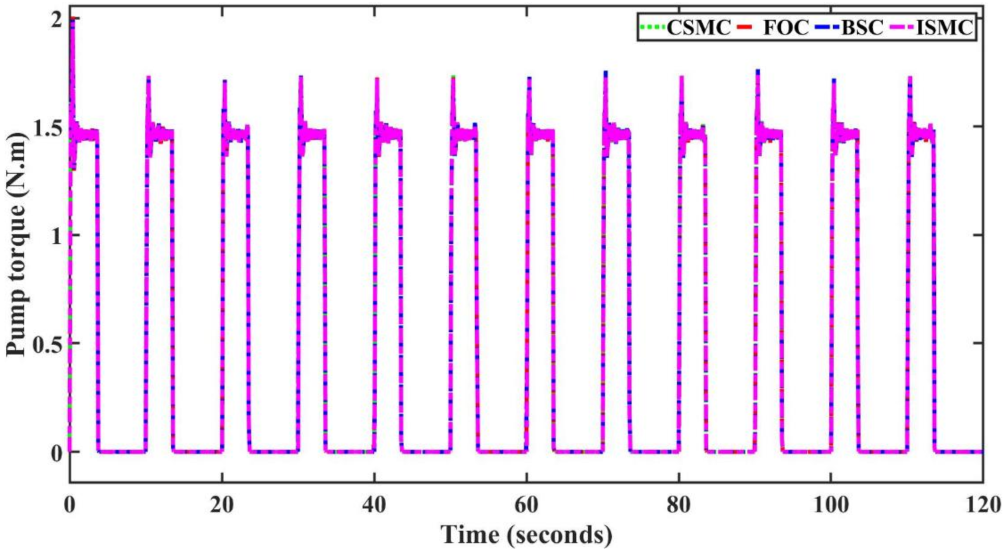

Fig. 35. Pump torque

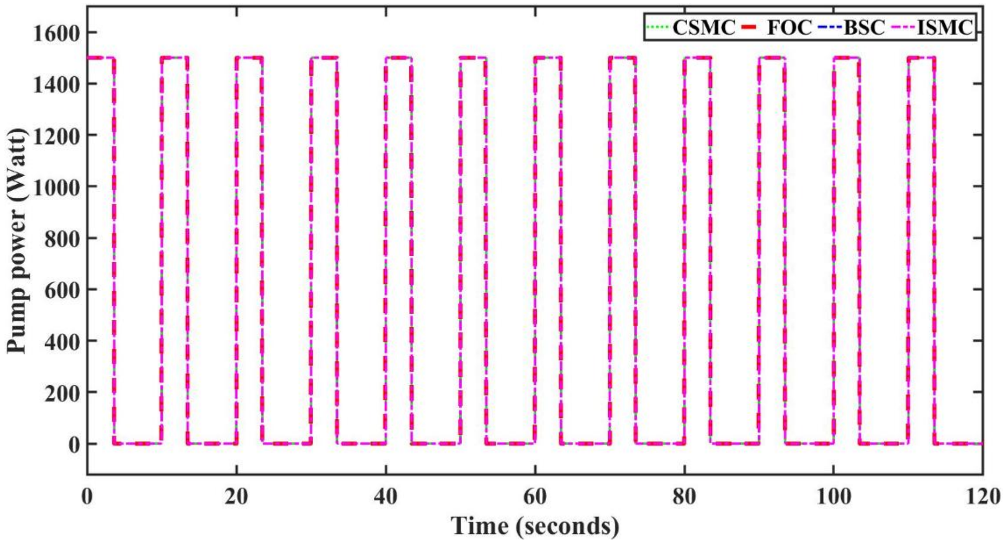

Fig. 36. Pump power

5.8. Power Flow Analysis

To evaluate the performance and the effectiveness of the power management system designed, the power produced by the generator, the power of the battery, the power consumed by the IM, and the excess power are compared for each control algorithm. Fig. 37 presents the power flow analysis under FOC, Fig. 38 covers CSMC, Fig. 39 covers BSC, and Fig. 40 covers ISMC. As presented in the figures, regardless of the control algorithm implemented for the MSC, the designed power management system has managed to achieve a stable power flow between both the generator and the water pump while utilizing the battery efficiently. Table 2 presents the time periods during which the system switches between different operation modes.

Table 2. Operation modes executed during different time periods

Time periods	Operation mode executed
[0-1.16], [12.3-13.47], [91.16-92.5]	Operation mode no.3 is executed. The tank is not full. The Pump is powered by the generated power, while excess power charges the battery
[1.16-3.6], [10-12.3], [20.4-23.47], [30-33.47], [40-43.3], [50-53.44], [60-63.4], [79.85-83.4], [90-91.16]	Operation mode no.5 is executed. The tank is not full. Generated power is not adequate for the pump. The shortage is covered by the battery
[3.6-10], [13.47-19.18], [23.47-30], [33.47-40], [43.3-50], [53.44-60], [63.47-66.84], [83.4-86.98]	Operation mode no.2 is executed. The tank is full. While the generated power charges the battery.
[19.18-20], [66.84-70], [73.47-79.85], [86.89-90], [93-100], [103.5-110], [113.5-120]	Operation mode no.1 is executed. The tank is full. While the battery is fully charged.
[20-20.4], [70-73.47], [92.5-93.5], [100-103.5], [110-113.5]	Operation mode no.4 is executed. The tank is not full. Generated power is adequate for the pump. The battery is fully charged.

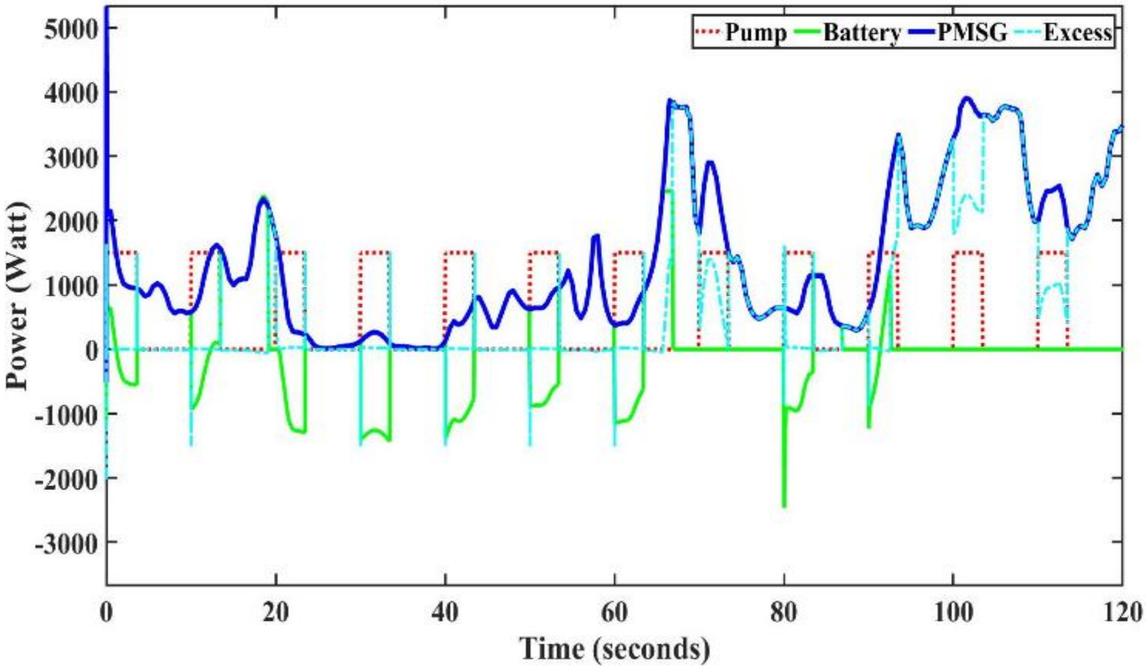

Fig. 37. System power flow under FOC

5.9. Convergence Time Analysis

To further investigate the time response of the system under the studied control algorithms, a step wind speed signal (Fig. 41) is used to evaluate the behaviour of the system. To see which control algorithm has faster response, settling time with 2% tolerance band of each is examined and compared at start [0-0.4], when wind speed increases [5-5.6], and when it also decreases [9-9.5]. The electromagnetic torque (Fig. 42), the quadrature current component (Fig. 43), and the active power of the PMSG are focused (Fig. 44). Settling time analysis shown in Table 3.

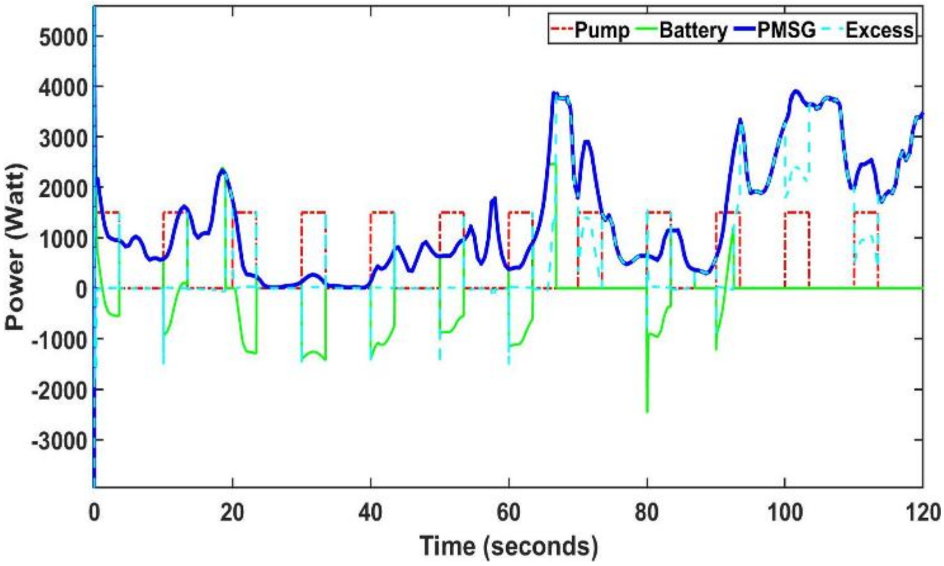

Fig. 38. System power flow under CSMC

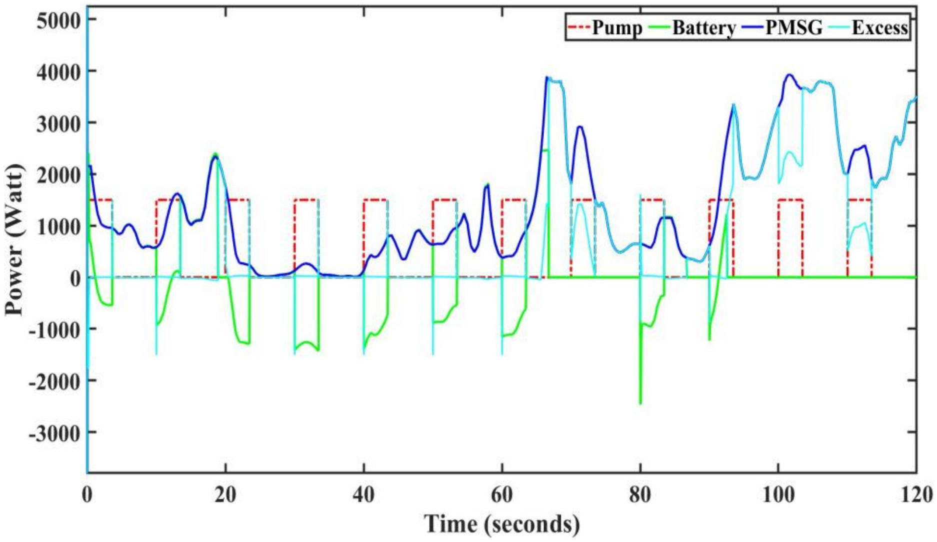

Fig. 39. System power flow under BSC

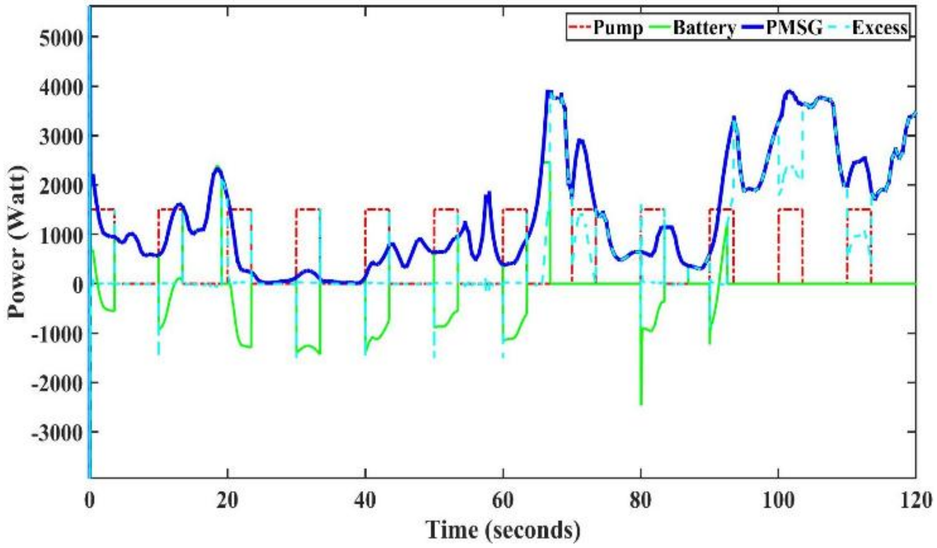

Fig. 40. System power flow under ISMC

Table 3. Settling time analysis

	FOC	CSMC	BSC	ISMC
$T_{\varepsilon mG}$	[0-0.4] 0.2878 sec	[0-0.4] 0.0459 sec	[0-0.4] 0.0032 sec	[0-0.4] 0.00155 sec
	[5-5.6] 0.4217 sec	[5-5.6] 0.094 sec	[5-5.6] 0.0055 sec	[5-5.6] 0.0029 sec
	[9-9.5] 0.3561 sec	[9-9.5] 0.0776 sec	[9-9.5] 0.0072 sec	[9-9.5] 0.0025 sec
i_Q	[0-0.4] 0.382 sec	[0-0.4] 0.0042 sec	[0-0.4] 0.0011 sec	[0-0.4] 0.0007 sec
	[5-5.6] 0.4405 sec	[5-5.6] 0.0933 sec	[5-5.6] 0.0057 sec	[5-5.6] 0.0033 sec
	[9-9.5] 0.4483 sec	[9-9.5] 0.0756 sec	[9-9.5] 0.0048 sec	[9-9.5] 0.0029 sec
P_G	[0-0.4] 0.4014 sec	[0-0.4] 0.0773 sec	[0-0.4] 0.00635 sec	[0-0.4] 0.00251 sec
	[5-5.6] 0.4890 sec	[5-5.6] 0.1320 sec	[5-5.6] 0.0091 sec	[5-5.6] 0.0041 sec
	[9-9.5] 0.2621 sec	[9-9.5] 0.1132 sec	[9-9.5] 0.00428 sec	[9-9.5] 0.0021 sec

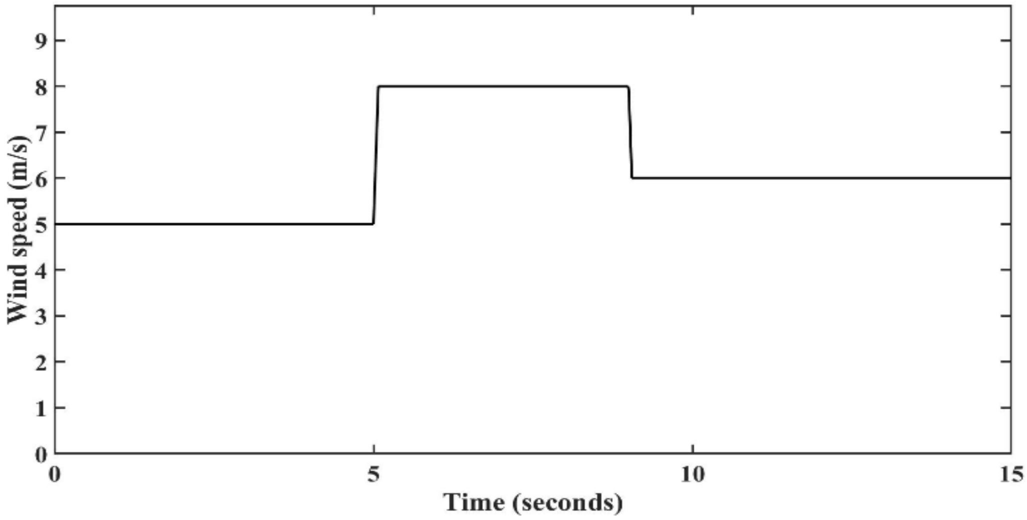

Fig. 41. Step wind speed

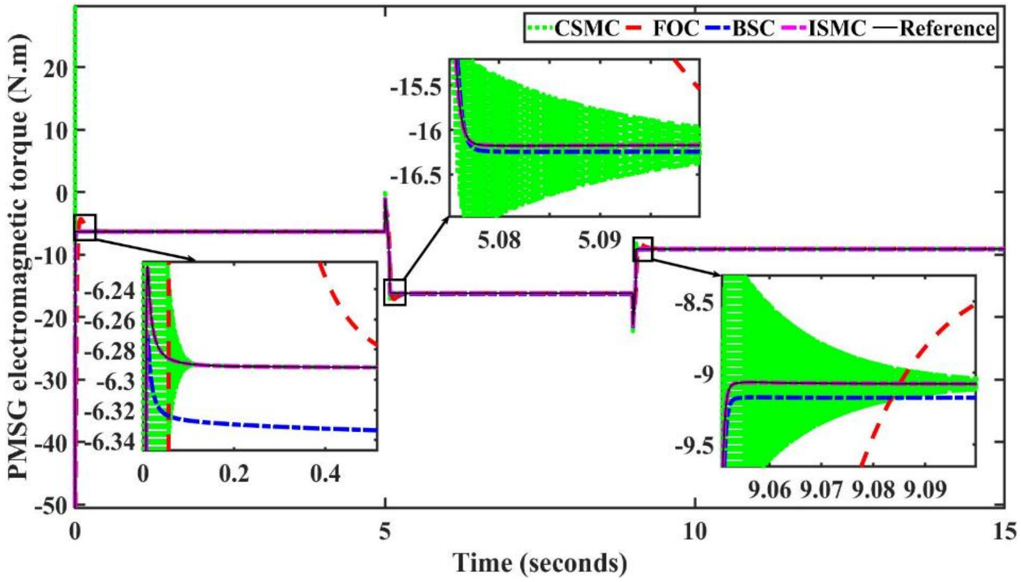

Fig. 42. PMSG electromagnetic torque

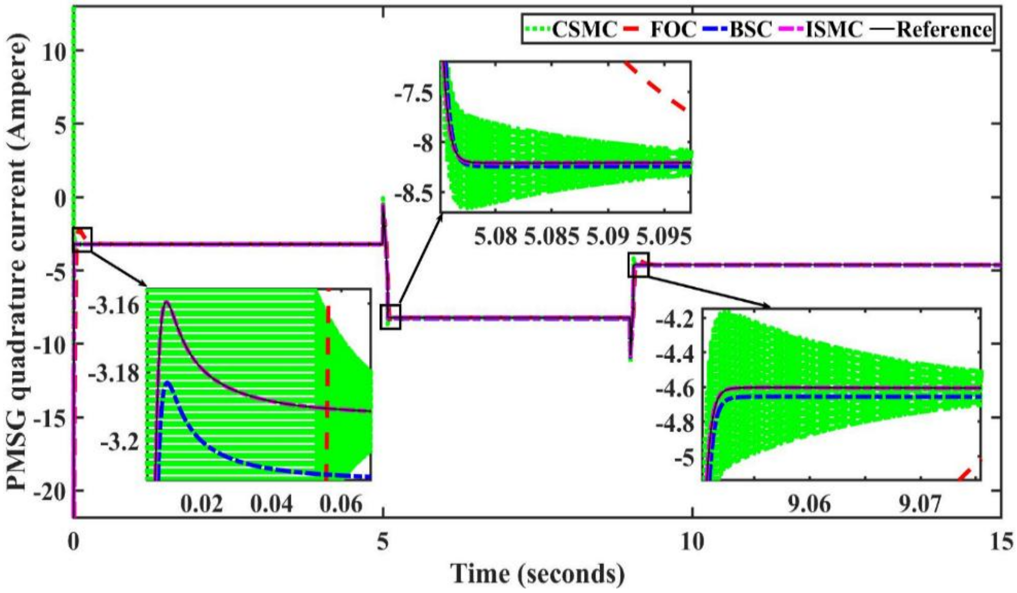

Fig. 43. PMSG quad current component

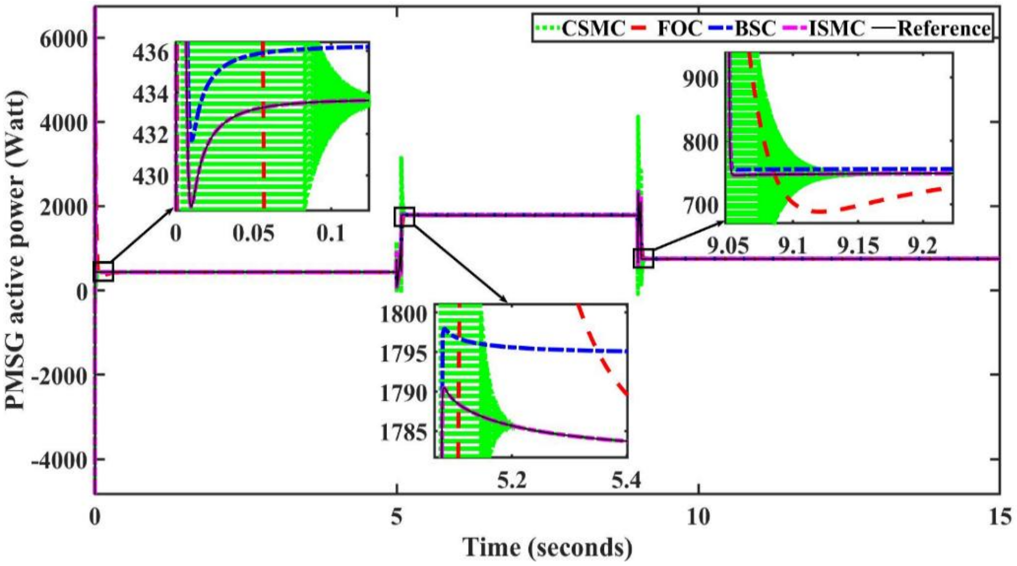

Fig. 44. PMSG active power

6. Conclusion

This study evaluated the effectiveness of four control strategies-Field-Oriented Control (FOC), Classical Sliding Mode Control (CSMC), Backstepping control (BSC), and a new Improved Sliding Mode Control (ISMC)-for regulating the performance of the generation unit in a WECS-based irrigation pumping system. A comprehensive set of performance assessments was conducted using MATLAB/Simulink under identical operating conditions to ensure a fair and objective comparison. The results indicate that, although FOC benefits from structural simplicity, it exhibits the slowest dynamic response. In contrast, CSMC provides faster convergence but suffers from pronounced oscillatory behavior, leading to increased current harmonics, as evidenced by the Total Harmonic Distortion (THD) analysis of the PMSG stator currents. The proposed ISMC demonstrates a substantial improvement over both conventional approaches, achieving a THD reduction of 52% relative to FOC, 72% relative to CSMC and 36% relative to BSC, thereby confirming its superior harmonic suppression capability. Moreover, convergence time analysis reveals that the ISMC attains the fastest dynamic response, with an approximately 99% reduction in settling time compared to FOC, about a 95% reduction compared to CSMC, and 51% compared to BSC. These results directly reflect the effectiveness of the improved control formulation in mitigating chattering effects while maintaining robustness and fast trajectory convergence. Consequently, the proposed ISMC emerges as the most effective control strategy among the evaluated methods, simultaneously ensuring rapid dynamic response and high-quality current waveforms. In addition, the implemented power management strategy successfully maintains balanced power flow among the PMSG, battery energy storage system, and irrigation load, thereby enhancing the overall stability, reliability, and efficiency of the standalone WECS. These findings highlight the suitability of the proposed ISMC framework for renewable energy-driven pumping applications operating under variable and uncertain wind conditions.

Future works will focus on expanding the system to include other types of renewable energy sources (PV solar panels and fuel cells [57]). Different optimization algorithms [58] for the gains of the control law will be examined to improve the dynamic response of the control algorithm. The proposed control algorithm will be modified, improved and applied to other types of generators such as doubly fed induction generators (DFIG), hybrid excitation synchronous generator (HESG) [59] and Self Excited Synchronous Generator (SESG) [60].

Abbreviations and Symbols

MSC	Machine side converter	$\boldsymbol{\nu}_{Ϙ}^{*}, ί_{Ϙ}^{*}$	Ref values of the quad component of the PMSG stator voltage and current
IMC	Induction motor converter	$\boldsymbol{\nu}_{Ϙ}, ί_{Ϙ}$	Actual values of the quad component of the PMSG stator voltage and current
IM	Induction motor	$\boldsymbol{\nu_a}^{*}, \boldsymbol{\nu_b}^{*}, \boldsymbol{\nu_c}^{*}$	Ref values of PMSG 3-$\boldsymbol{\varphi}$ stator voltage
PMS	Power management system	$ί_{\boldsymbol{a}}, ί_{\boldsymbol{b}}, ί_{\boldsymbol{c}}$	Actual values of PMSG 3-$\boldsymbol{\varphi}$ stator current
$\mathrm{P}_{\boldsymbol{aero}}$	Wind kinetic power	$\mathbf{T}_{\boldsymbol{\varepsilon mG}}, \mathbf{T}_{\boldsymbol{\varepsilon mG}}^{*}$	Actual and ref values of the electromagnetic torque of PMSG
$\boldsymbol{\rho_a}, \boldsymbol{\rho_w}$	Air and water density	$\boldsymbol{P_G}, \boldsymbol{P}_{\mathrm{M}}$	Number of pole pairs of PMSG and IM
$\boldsymbol{r}$	Radius of wind turbine's blades	$\mathrm{P}_{\boldsymbol{G}}, Ϙ_{\boldsymbol{G}}$	Real and imaginary powers of PMSG
$\boldsymbol{v_w}$	Wind speed	$\boldsymbol{\nu_{cb}}, \boldsymbol{\nu_{cs}}$	Voltages of the bulk capacitor and the surface capacitor
$\boldsymbol{v_{Cut\ in}}, \boldsymbol{v_{Cut\ off}}$	Cut in and cut off wind speeds	$\boldsymbol{C_b}, \boldsymbol{C_s}$	bulk capacitor and surface capacitor
$\boldsymbol{v_{rated}}$	Rated wind speed	$\boldsymbol{R_\tau}, \boldsymbol{R_\varepsilon}, \boldsymbol{R}_{\mathbf{S}}$	Terminal, surface, and end resistances
$\mathrm{P}_{\boldsymbol{T}}, \mathbf{T}_{\boldsymbol{T}}$	Wind turbine power and shaft torque	PI	Proportional-Integral controller
$\boldsymbol{C_p}, \boldsymbol{\lambda}, \boldsymbol{\beta}$	Wind turbine's power coefficient, tip speed ratio, and pitch angle	$\boldsymbol{L_\beta}$	Inductance of inductor-based filter used for battery current
TSR	Tip speed ratio MPPT method	$\boldsymbol{\nu_\beta}, ί_{\boldsymbol{\beta}}$	Battery voltage and current
$\boldsymbol{\lambda_i}$	Intermediate tip speed ratio	$\boldsymbol{P_\beta}, \boldsymbol{P_\beta}^{*}$	Actual and ref values of battery power
$\boldsymbol{\lambda_{opt}}$	Optimum tip speed ratio	$\boldsymbol{SOC}, \boldsymbol{SOC_{Min}}, \boldsymbol{SOC_{Max}}$	Battery state of charge, its min and max values
$\boldsymbol{\Omega_T}, \boldsymbol{\Omega_T}^{*}$	Wind turbine actual and ref angular speed	$\boldsymbol{\nu}_{\alpha\mathrm{I}}, \boldsymbol{\nu}_{\beta\mathrm{I}}$	Induction motor stator voltage in $\boldsymbol{\alpha}, \boldsymbol{\beta}$ ref frame
$\boldsymbol{G}$	Gearbox ratio	$\boldsymbol{\nu}_{\alpha\mathrm{II}}, \boldsymbol{\nu}_{\beta\mathrm{II}}$	Induction motor rotor voltages in $\boldsymbol{\alpha}, \boldsymbol{\beta}$ ref frame
$\boldsymbol{T_G}$	PMSG shaft torque	$ί_{\alpha\mathrm{I}}, ί_{\beta\mathrm{I}}$	Induction motor stator currents in $\boldsymbol{\alpha}, \boldsymbol{\beta}$ ref frame
$\boldsymbol{\theta_{\varepsilon G}}$	PMSG stator electrical angle	$ί_{\delta\mathrm{I}}, ί_{Ϙ\mathrm{I}}$	Induction motor stator currents in $\boldsymbol{d}, \boldsymbol{q}$ ref frame
$\boldsymbol{\Omega_\varepsilon}$	PMSG electrical angular speed	$ί_{\alpha\mathrm{II}}, ί_{\beta\mathrm{II}}$	Induction motor rotor currents in $\boldsymbol{\alpha}, \boldsymbol{\beta}$ ref frame

$\boldsymbol{\Omega_G}, \boldsymbol{\Omega_G}^*$	PMSG actual and ref angular speed	$\boldsymbol{R}_{\mathrm{I}}, \boldsymbol{R}_{\mathrm{II}}$	Induction motor stator and rotor resistances
$\boldsymbol{J_T}, \boldsymbol{J_G}, \boldsymbol{J}_{\mathrm{M}}$	Inertia of turbine, PMSG, and IM	$\boldsymbol{L}_{\mathrm{I}}, \boldsymbol{L}_{\mathrm{II}}, \mathrm{M}_{\mathrm{M}}$	Induction motor stator, rotor, and mutual inductances
$\boldsymbol{\varphi}_{\mathrm{M}}$	Permanent magnet flux	$\boldsymbol{\sigma}_{\mathrm{M}}$	Leakage factor of the IM
$\boldsymbol{R_S}, \boldsymbol{L_S}$	PMSG stator resistance and inductance	$\boldsymbol{\varphi}_{\alpha\mathrm{I}}, \boldsymbol{\varphi}_{\beta\mathrm{I}}$	Induction motor stator fluxes in $\boldsymbol{\alpha}, \boldsymbol{\beta}$ ref frame
$\boldsymbol{\nu_\delta}^*, \acute{\iota}_{\boldsymbol{\delta}}^*$	Ref values of the direct component of the PMSG stator voltage and current	$\boldsymbol{\varphi}_{\alpha\mathrm{II}}, \boldsymbol{\varphi}_{\beta\mathrm{II}}$	Induction motor rotor fluxes in $\boldsymbol{\alpha}, \boldsymbol{\beta}$ ref frame
$\boldsymbol{\nu_\delta}, \acute{\iota}_{\boldsymbol{\delta}}$	Actual values of the direct component of the PMSG stator voltage and current	$\boldsymbol{\Theta}_{\varepsilon I}$	IM stator electrical angle
		$\boldsymbol{\Omega}_{\varepsilon I}$	IM stator electrical angular speed
$\mathbf{T}_{\varepsilon m\mathrm{M}}, \mathbf{T}_{\varepsilon m\mathrm{M}}^*$	Actual and ref values of the electromagnetic torque of IM	PWM	Pulse width modulation
$\boldsymbol{\Omega}_{\mathrm{M}}, \boldsymbol{\Omega}_{\mathrm{M}}^*$	IM actual and ref angular speed	$\boldsymbol{\nu}_{a\mathrm{I}}^*, \boldsymbol{\nu}_{b\mathrm{I}}^*, \boldsymbol{\nu}_{c\mathrm{I}}^*$	Ref values of IM 3-$\boldsymbol{\varphi}$ stator voltage
$\boldsymbol{\nu}_{\delta\mathrm{I}}^*, \acute{\iota}_{\delta\mathrm{I}}^*$	Ref values of the direct component of IM stator voltage and current	$\acute{\iota}_{a\mathrm{I}}, \acute{\iota}_{b\mathrm{I}}, \acute{\iota}_{c\mathrm{I}}$	Actual values of IM 3-$\boldsymbol{\varphi}$ stator current
$\boldsymbol{\nu}_{\delta\mathrm{I}}, \acute{\iota}_{\delta\mathrm{I}}$	Actual values of the direct component of IM stator voltage and current	$\boldsymbol{P}_{\Pi}, \boldsymbol{P}_{\Pi}^*$	Actual and ref values of the water pump power
$\boldsymbol{\nu}_{ϙ\mathrm{I}}^*, \acute{\iota}_{ϙ\mathrm{I}}^*$	Ref values of the quad component of IM stator voltage and current	$\boldsymbol{P}_{\Pi\_nom}$	Nominal power of the pump
$\boldsymbol{\nu}_{ϙ\mathrm{I}}, \acute{\iota}_{ϙ\mathrm{I}}$	Actual values of the quad component of IM stator voltage and current	$\boldsymbol{K}_{\Pi}$	Water pump speed-torque coefficient
$\boldsymbol{\varphi}_{\delta\mathrm{II}}, \boldsymbol{\varphi}_{\delta\mathrm{II}}^*$	Actual and Ref values of the direct component of IM rotor flux	$\boldsymbol{\eta}$	Efficiency of the pump
abc/dq	Park transformation	$\boldsymbol{Q}_{\Pi}$	Flow rate of the pump
dq/abc	Inverse Park transformation	$\boldsymbol{g}$	Gravity acceleration
$\boldsymbol{H_w}^*, \boldsymbol{H_w}$	Ref and measured water stage inside the tank	$\acute{\iota}_{III}$	the current supplied to the DC link by the DC/DC converter
$\boldsymbol{A_t}$	Water tank area	$\boldsymbol{\nu}_{III}$	The voltage supplied to the DC/DC converter by the battery
$\boldsymbol{Q}_{in}, \boldsymbol{Q}_{out}$	the Inflow and the outflow of the tank	$\boldsymbol{\nu}_{\mathbf{eq}}, \boldsymbol{\nu}_{\mathbf{n}}$	Equivalent and switching components of the control law
$\boldsymbol{\nu}_{DC}, \acute{\iota}_{DC}, \boldsymbol{C}$	DC link voltage, current, and capacity	Υ	Candidate Lyapunov functions of CSMC and ISMC
$\boldsymbol{P}_{DC}^*, \acute{\iota}_{DC}^*$	Ref values of DC link power and DC link current	$\boldsymbol{\zeta}_{\delta n1}, \boldsymbol{\zeta}_{ϙn1}$	CSMC constants
$\acute{\iota}_{\mathrm{I}}$	The output DC current of the MSC	$\boldsymbol{\zeta}_{\delta n2}, \boldsymbol{\zeta}_{ϙn2},$ $\boldsymbol{\zeta}_{\delta n3}, \boldsymbol{\zeta}_{ϙn3}$	ISMC constants
$\acute{\iota}_{\mathrm{II}}$	The DC current withdrawn by IMC	σ	Candidate Lyapunov function of BSC
MC	Modulation coefficient	$\xi_{\Omega}, \xi_{\delta}, \xi_{ϙ}$	BSC constants

Appendix

System parameters

Parameter	Value	Parameter	Value
λ_{opt}	8.1	L_I, L_{II}, M_M	0.1164,0.1164,0.1113 H
r	2m	σ_M	0.0857
ρ_a	1.22 kg/m3	R_I, R_{II}	1.411,1.045 Ω
ρ_w	1 kg/L	Battery rated voltage	240 V
J_G	0.0099 kg·m2	ν_{DC}^*, C	550 V, 2200 µF
J_M	0.34 kg·m2	Battery capacity	50 Ah
G	3.83	C_b, C_s	8.8373 F,82.1 mF
φ_M	0.50 Wb	L_β	30 mH
P_G, P_M	4,2	$R_{\tau,} R_\varepsilon, R_S$	2.75,3.75,3.75 mΩ
R_S, L_S	0.82 Ω, 15.1 mH	DOD	60%
$P_{G_}$nom	3.85KW	η_{Battery}	85 %
φ_{II}^*	0.924 Wb		

Author Contribution: All authors contributed equally to the main contributor to this paper. All authors read and approved the final paper.

Funding: This research received no external funding.

Conflicts of Interest: The authors declare no conflict of interest.

References

[1] S. I. Salah, M. Eltaweel, and C. Abeykoon, “Towards a sustainable energy future for Egypt: A systematic review of renewable energy sources, technologies, challenges, and recommendations,” *Cleaner Engineering and Technology*, vol. 8, p. 100497, 2022, https://doi.org/10.1016/j.clet.2022.100497.

[2] B. Loza, L. I. Minchala, D. Ochoa-Correa, and S. Martinez, “Grid-Friendly Integration of Wind Energy: A review of power forecasting and frequency control techniques,” *Sustainability*, vol. 16, no. 21, p. 9535, 2024, https://doi.org/10.3390/su16219535.

[3] S. BalaKumar, M. Lemma, and M. Godato, “Solar-powered ANN-based MPPT with zeta converter for BLDC motor water pumping in rural Ethiopia for sustainable agriculture,” *Discover Sustainability*, vol. 6, no. 1, p. 140, 2025, https://doi.org/10.1007/s43621-025-00893-8.

[4] A. Chatterjee, “Wind Power Generation for Isolated Loads with IoT-based Smart Load Controller,” *Journal of Fuzzy Systems and Control*, vol. 2, no. 2, pp. 92-96, 2024, https://doi.org/10.59247/jfsc.v2i2.210.

[5] O. Alabedalkhamis, “Study the types of electrical generators used in wind turbines,” *Bingöl University Journal of Technical Sciences*, 2025, https://doi.org/10.5281/zenodo.18268871.

[6] O. Alabedalkhamıs and H. Alptekin, “Methods of Control for Generators that Used in Wind Turbines,” *Harran Üniversitesi Mühendislik Dergisi*, vol. 10, no. 4, pp. 255–271, 2025, https://doi.org/10.46578/humder.1700888.

[7] V. Singh, G. Selvaraj, and K. Rajashekara, “Enhanced Volts-per-Hertz Sensorless Starting of Permanent Magnet Motor with Heavy Loads in Long-Cable Subsea Applications,” *Energies*, vol. 17, no. 4, p. 957, 2024, https://doi.org/10.3390/en17040957.

[8] S. Foti, A. Testa, G. Baia, C. S. Staines, and C. Caruana, “Fault detection on induction machines operated in V/f scalar control,” *IET Conference Proceedings*, vol. 2024, no. 3, pp. 138-145, 2024, https://doi.org/10.1049/icp.2024.2149.

[9] S. Mencou, M. B. Yakhlef, and E. B. Tazi, “Advanced control of induction motors (2019–2025): A comprehensive review of strategies, algorithms and sensorless techniques,” *e-Prime - Advances in Electrical Engineering Electronics and Energy*, vol. 14, p. 101098, 2025, https://doi.org/10.1016/j.prime.2025.101098.

[10] M. Aimene, A. Payman, and B. Dakyo, “Comparative Study between Flatness-Based and Field-Oriented Control Methods of a Grid-Connected Wind Energy Conversion System,” *Processes*, vol. 10, no. 2, p. 378, 2022, https://doi.org/10.3390/pr10020378.

[11] M. Alzayed, Y. Farajpour and H. Chaoui, “Simplified Current Sensorless Maximum Power Extraction for Wind Energy Conversion Systems,” *IEEE Access*, vol. 10, pp. 104686-104695, 2022, https://doi.org/10.1109/ACCESS.2022.3210951.

[12] H. Gasmi, H. Benbouhenni, N. Bizon and S. Mendaci, “Field-Oriented Control Based on Nonlinear Techniques for Wind Energy Conversion Systems,” *2023 15th International Conference on Electronics, Computers and Artificial Intelligence (ECAI)*, pp. 1-7, 2023, https://doi.org/10.1109/ECAI58194.2023.10194068.

[13] A. Dani, Z. Mekrini, M. E. Mrabet, and M. Boulaala, “Maximum Power Point Tracking and Field-Oriented Control strategies applied to PMSG-Based WECS,” *Digital Technologies and Applications*, pp. 506–516, 2024, https://doi.org/10.1007/978-3-031-68650-4_48.

[14] D. B. Parmar and A. K. Giri, “Integration of field-oriented and steady-state linear Kalman filter control in PMSG-based grid-connected system for improving voltage control and power balance operation,” *Electrical Engineering*, vol. 107, no. 7, pp. 8803–8817, 2024, https://doi.org/10.1007/s00202-024-02456-y.

[15] A. Halmous, Y. Oubbati, and M. Lahdeb, “Control optimization of grid-connected PMSG wind turbine with OOBO algorithm and cascade PI-PID controller,” *Electrical Engineering*, vol. 106, no. 6, pp. 7073–7087, 2024, https://doi.org/10.1007/s00202-024-02401-z.

[16] S. B. Joseph, E. G. Dada, A. Abidemi, D. O. Oyewola, and B. M. Khammas, “Metaheuristic algorithms for PID controller parameters tuning: review, approaches and open problems,” *Heliyon*, vol. 8, no. 5, p. e09399, 2022, https://doi.org/10.1016/j.heliyon.2022.e09399.

[17] Ł. Lemieszewski and P. Puzio, “Optimization of PID controller settings using the Ziegler–Nichols method in pneumatic pressure control systems,” *Procedia Computer Science*, vol. 270, pp. 5177–5186, 2025, https://doi.org/10.1016/j.procs.2025.09.645.

[18] A. A. Arwa, M. A. Ietiqal, J. Y. Salam, and T. and E. R. O. M. of E. Iraq Baghdad 10001, “Bald eagle search algorithm based PI control method for speed control of BLDC motor drives,” *AIMS Electronics and Electrical Engineering*, vol. 9, no. 4, pp. 565-588, 2025, https://www.aimspress.com/article/doi/10.3934/electreng.2025025.

[19] S. Yan, Y. Yang, S. Y. Hui and F. Blaabjerg, “A Review on Direct Power Control of Pulsewidth Modulation Converters,” *IEEE Transactions on Power Electronics*, vol. 36, no. 10, pp. 11984-12007, 2021, https://doi.org/10.1109/TPEL.2021.3070548.

[20] A. Mehaouchi, M. Bouzidi, B. Rabhi, H. Abu-Rub, S. Barkat and A. Boubekri, “Simplified Direct Power Control for Grid Connected Multilevel Diode Clamped Converter,” *IEEE Open Journal of the Industrial Electronics Society*, vol. 6, pp. 1461-1475, 2025, https://doi.org/10.1109/OJIES.2025.3600577.

[21] M. D. Constantinescu, M. Popescu, G. -E. Subtirelu and I. -C. Toma, “Application of the Direct Power Control in a Three-Phase Shunt Active Power Filter System,” *2023 International Conference on Electromechanical and Energy Systems (SIELMEN)*, pp. 1-6, 2023, https://doi.org/10.1109/SIELMEN59038.2023.10290862.

[22] B. Essoussi, A. Moutabir, B. Bensassi, A. Ouchatti, Y. Zahraoui, and B. Benazza, “Power Quality Improvement using a New DPC Switching Table for a Three-Phase SAPF,” *International Journal of Robotics and Control Systems*, vol. 3, no. 3, pp. 510–529, 2023, https://doi.org/10.31763/ijrcs.v3i3.1042.

[23] T. Trivedi, R. Jadeja, P. Bhatt, and A. Ved, “Implementation of modified switching table for direct power control of shunt active power filter,” *Australian Journal of Electrical & Electronics Engineering*, vol. 20, no. 2, pp. 147–163, 2022, https://doi.org/10.1080/1448837X.2022.2113171.

[24] A. Taibi, K. Hartani, T. M. Chikouche, and N. Aouadj, “Fuzzy Logic-Based DPC for PWM rectifiers: enhancing power quality and advancing the sustainable development goals,” *Journal of Lifestyle and SDGs Review*, vol. 5, no. 4, p. e06118, 2025, https://doi.org/10.47172/2965-730X.SDGsReview.v5.n04.pe06118.

[25] M. A. H. Mujammal, A. Moualdia, G. Lorenzini, S. Boulkhrachef, P. Wira, and M. A. Albasheri, “Three-Phase PWM Rectifier Control: Enhanced Direct Power Control with Neural Networks from Theory to Superior Reality Performance,” *Journal Européen Des Systèmes Automatisés*, vol. 57, no. 6, pp. 1743–1752, 2024, https://doi.org/10.18280/jesa.570622.

[26] H. Salime, B. Bossoufi, S. Motahhir, and Y. E. Mourabit, “A novel combined FFOC-DPC control for wind turbine based on the permanent magnet synchronous generator,” *Energy Reports*, vol. 9, pp. 3204–3221, 2023, https://doi.org/10.1016/j.egyr.2023.02.012.

[27] L. Shi and S. Jin, “Direct Power Control and Space Vector Modulation-Based Direct Power Control for brushless Doubly-Fed Reluctance Generator,” *IEEJ Transactions on Electrical and Electronic Engineering*, vol. 18, no. 8, pp. 1371–1378, 2023, https://doi.org/10.1002/tee.23859.

[28] M. Yessef *et al.*, “Two different controllers-based DPC of the doubly-fed induction generator with real-time implementation on dSPACE 1104 controller board,” *Measurement and Control*, vol. 57, no. 8, pp. 1123–1145, 2024, https://doi.org/10.1177/00202940241236288.

[29] A. Benevieri, M. Marchesoni, M. Passalacqua, P. Pozzobon, and L. Vaccaro, “Synchronous DTC for torque sub-harmonic reduction in low switching frequency induction motor drives,” *Control Engineering Practice*, vol. 154, p. 106133, 2024, https://doi.org/10.1016/j.conengprac.2024.106133.

[30] M. Azab, “Low-Cost DTC drive using Four-Switch inverter for low power ranges,” *Vehicles*, vol. 6, no. 2, pp. 895–919, 2024, https://doi.org/10.3390/vehicles6020043.

[31] B. Mokhtari, “Enhancement Ripples of a Direct Torque Control Applied to a Permanent Magnet Synchronous Motor by Using a Four-Level Multicellular Inverter and a New Reduced Switching Table,” *Revue Roumaine Des Sciences Techniques - Série Électrotechnique Et Énergétique*, vol. 69, no. 2, pp. 207–212, 2024, https://doi.org/10.59277/RRST-EE.2024.2.15.

[32] Y. Sahri *et al.*, “Effectiveness analysis of twelve sectors of DTC based on a newly modified switching table implemented on a wind turbine DFIG system under variable wind velocity,” *Ain Shams Engineering Journal*, vol. 14, no. 11, p. 102221, 2023, https://doi.org/10.1016/j.asej.2023.102221.

[33] C. Fahassa, Y. Zahraoui, M. Akherraz, M. Kharrich, E. E. Elattar, and S. Kamel, “Induction motor DTC performance improvement by inserting fuzzy logic controllers and Twelve-Sector neural network switching table,” *Mathematics*, vol. 10, no. 9, p. 1357, 2022, https://doi.org/10.3390/math10091357.

[34] M. H. Holakooie, G. Iwanski and T. Miazga, “Five-Dimensional Switching-Table-Based Direct Torque Control of Six-Phase Drives,” *IEEE Transactions on Power Electronics*, vol. 37, no. 12, pp. 15260-15271, 2022, https://doi.org/10.1109/TPEL.2022.3189876.

[35] H. Dewangan, S. V. S. P. Kumar Ch, S. Venu and S. Jain, “Modelling and Implementation of Space Vector Modulation Based Direct Torque Control in Stator Flux Reference Frame for Induction Motor Drive,” *2023 IEEE 3rd International Conference on Sustainable Energy and Future Electric Transportation (SEFET)*, pp. 1-6, 2023, https://doi.org/10.1109/SeFeT57834.2023.10244954.

[36] A. O. Deab, K. Karthikumar, M. Karuppiah, and P. a. G. Sankar, “A new optimal space vector modulation with DTC switching strategy for induction motor control,” *International Journal of Applied Power Engineering (IJAPE)*, vol. 13, no. 4, p. 862, 2024, http://doi.org/10.11591/ijape.v13.i4.pp862-873.

[37] D. V. Makwana, N. B. Panchal, V. M. Parmar, P. A. Upadhyay, M. G. Jadeja, “LSTM-ANN Intelligent Control based on Space Vector Modulated DTC for induction Motor Drive,” *International Journal of Intelligent Systems and Applications in Engineering*, vol. 12, no. 4, pp. 2254–2259, 2024, https://www.ijisae.org/index.php/IJISAE/article/view/6602.

[38] M. A. Mossa, O. Gam, and N. Bianchi, “Performance Enhancement of a Hybrid Renewable Energy System Accompanied with Energy Storage Unit Using Effective Control System,” *International Journal of Robotics and Control Systems*, vol. 2, no. 1, pp. 140–171, 2022, https://doi.org/10.31763/ijrcs.v2i1.599.

[39] R. Mohamed, M. A. Mossa, and A. El-Gaafary, “Performance enhancement of a variable speed permanent magnet synchronous generator used for renewable energy application,” *International Journal of Robotics and Control Systems*, vol. 3, no. 3, pp. 530–560, 2023, https://doi.org/10.31763/ijrcs.v3i3.1031.

[40] M. Abbasi and N. Sadati, “Multiple model predictive control for offshore wind turbines operating in the full-load range,” *Asian Journal of Control*, vol. 27, no. 4, pp. 2023–2036, 2024, https://doi.org/10.1002/asjc.3549.

[41] A. Herizi, R. Rouabhi, and A. Zemmit, “Speed control of doubly fed induction motor using backstepping control with interval type-2 fuzzy controller,” *Diagnostyka*, vol. 24, no. 3, pp. 1–8, 2023, https://doi.org/10.29354/diag/166460.

[42] H. Gharsallaoui and M. Benrejeb, “Electronic Throttle Valve Backstepping Control Based Sliding Mode Triangular Observer,” *2025 International Conference on Control, Automation and Diagnosis (ICCAD)*, pp. 1-6, 2025, https://doi.org/10.1109/ICCAD64771.2025.11099350.

[43] B. Majout *et al.*, “A review on popular control applications in wind Energy Conversion System based on Permanent Magnet Generator PMSG,” *Energies*, vol. 15, no. 17, p. 6238, 2022, https://doi.org/10.3390/en15176238.

[44] H. Salime, B. Bossoufi, Y. E. Mourabit, and S. Motahhir, “Robust nonlinear adaptive control for power quality enhancement of PMSG wind turbine: experimental Control validation,” *Sustainability*, vol. 15, no. 2, p. 939, 2023, https://doi.org/10.3390/su15020939.

[45] M. M. Alhato, S. Bouallègue, H. Rezk, “Modeling and performance improvement of direct power control of doubly-fed induction generator based wind turbine through second-order sliding mode control approach,” *Mathematics*, vol. 8, no. 11, p. 2012, 2020, https://doi.org/10.3390/math8112012.

[46] N. Z. Laabidine, B. Bossoufi, I. E. Kafazi, C. E. Bekkali, and N. E. Ouanjli, “Robust adaptive super twisting algorithm sliding mode control of a wind system based on the PMSG generator,” *Sustainability*, vol. 15, no. 14, p. 10792, 2023, https://doi.org/10.3390/su151410792.

[47] Z. Liao, Y. Hao, T. Guo, B. Lv, and Q. Wang, “Second-Order sliding mode control of permanent magnet synchronous motor based on singular perturbation,” *Energies*, vol. 15, no. 21, p. 8028, 2022, https://doi.org/10.3390/en15218028.

[48] X. Wang, Z. Liu, P. Zhou, B. Jia, R. Li, and Y. Xu, “A saturation adaptive nonlinear integral sliding mode controller for ship permanent magnet propulsion motors,” *Journal of Marine Science and Engineering*, vol. 13, no. 5, p. 976, 2025, https://doi.org/10.3390/jmse13050976.

[49] M. A. Mossa, H. Echeikh, and A. Iqbal, “Enhanced control technique for a sensor-less wind driven doubly fed induction generator for energy conversion purpose,” *Energy Reports*, vol. 7, pp. 5815–5833, 2021, https://doi.org/10.1016/j.egyr.2021.08.183.

[50] A. L. Haridy, E. H. Abdelhameed, Y. Chen, E. A. Mohamed, M. Abouheaf, and A.-A. A. Mohamed, “Optimal control design for enhancing the maximum power extraction from PMSG-based grid connected wind turbines,” *Journal of Engineering Research*, 2026, https://doi.org/10.1016/j.jer.2026.01.009.

[51] M. A. A. Mohamed, T. F. Yu, G. Ramsden, J. Marco, and T. Grandjean, “Advancements in parameter estimation techniques for 1RC and 2RC equivalent circuit models of lithium-ion batteries: A comprehensive review,” *Journal of Energy Storage*, vol. 113, p. 115581, 2025, https://doi.org/10.1016/j.est.2025.115581.

[52] T. B. D. Santos, I. Oliani, R. Figueiredo, D. Albieiro, A. Pelizari and A. J. Sguarezi Filho, “Robust Finite Control Set Model Predictive Current Control for Induction Motor Using Deadbeat Approach in Stationary Frame,” *IEEE Access*, vol. 11, pp. 13067-13078, 2023, https://doi.org/10.1109/ACCESS.2022.3223385.

[53] C.-W. Ding and P.-C. Tung, “A New Approach to Field-Oriented Control That Substantially Improves the Efficiency of an Induction Motor with Speed Control,” *Applied Sciences*, vol. 15, no. 9, p. 4845, 2025, https://doi.org/10.3390/app15094845.

[54] T. Ramasamy, A. A. Basheer, M.-H. Tak, Y.-H. Joo, and S.-R. Lee, “An effective DC-Link voltage control strategy for Grid-Connected PMVG-Based wind energy conversion system,” *Energies*, vol. 15, no. 8, p. 2931, 2022, https://doi.org/10.3390/en15082931.

[55] J. Xu, P. Feng, J. Gong, S. Li, G. Jiang, and H. Yang, “Low-Voltage Ride-Through Strategy to Doubly-Fed Induction Generator with Passive Sliding Mode Control to the Rotor-Side Converter,” *Energies*, vol. 17, no. 17, p. 4439, 2024, https://doi.org/10.3390/en17174439.

[56] Z. Hua, H. Ruan, D. Tu, X. Zhang, and K. Zhang, “Research on motion control of underwater robot based on improved active Disturbance rejection Control,” *Lecture notes in computer science*, pp. 61-73, 2023, https://doi.org/10.1007/978-981-99-6501-4_6.

[57] M. M. Al-Sawalha, H. Yasmin, S. Muhammad, Y. Khan, and R. Shah, “Optimal power management of a stand-alone hybrid energy management system: Hydro-photovoltaic-fuel cell,” *Ain Shams Engineering Journal*, vol. 15, no. 12, p. 103089, 2024, https://doi.org/10.1016/j.asej.2024.103089.

[58] Z. Liu, W. Li, and H. Wang, “Optimizing sliding mode control with hybrid enhanced particle swarm optimization: a study on enhancing wheeled mobile robot performance,” *Physica Scripta*, vol. 100, no. 7, p. 075254, 2025, https://doi.org/10.1088/1402-4896/ade646.

[59] A. Mseddi *et al*., “Exploring the Potential of Hybrid Excitation Synchronous Generators in Wind Energy: A Comprehensive Analysis and Overview,” *Processes*, vol. 12, no. 6, p. 1186, 2024, https://doi.org/10.3390/pr12061186.

[60] Y. Yamamoto, S. Kobayashi and K. -I. Yamashita, “Effects of System Parameters on the Steady-State Characteristics of a Wind Turbine Generator Based on Self-Excited Synchronous Generator for HVDC-Connected Wind Power Plants,” *2021 24th International Conference on Electrical Machines and Systems (ICEMS)*, pp. 2223-2227, 2021, https://doi.org/10.23919/ICEMS52562.2021.9634257.